



**TECHNISCHE
UNIVERSITÄT
WIEN**
Vienna University of Technology

DIPLOMARBEIT

**POLARIZATION-SENSITIVE ADAPTIVE OPTICS
ENHANCED OPTICAL COHERENCE
TOMOGRAPHY WITH DYNAMIC FOCUS**

Ausgeführt am

Institut für Angewandte Physik
der Technischen Universität Wien

unter der Anleitung von

Ao.Univ.Prof. Dipl.-Ing. Dr.techn. Martin Gröschl

in Zusammenarbeit mit

Assoc. Prof. Priv.-Doz. Dipl.-Ing. Dr. Michael Pircher

Zentrum für Medizinische Physik und Biomedizinische Technik
der Medizinischen Universität Wien

durch

Matthias Rechenmacher BSc

Handelskai 300a/2/2/8

1020 Wien

October 28, 2014

STATUTORY DECLARATION

I declare that I have authored this thesis independently, that I have not used other than the declared sources / resources, and that I have explicitly marked all material which has been quoted either literally or by content from the used sources.

Vienna, the 28. October 2014

Matthias Rechenmacher

Acknowledgements

First, I would like to thank Prof. Michael Pircher from the Medical University of Vienna who gave me the opportunity to work and research at the Center of Medical Physics and Biomedical Engineering. I want to thank him for his extensive support, for the time and effort he invested in my work. I also want to thank my supervisor Prof. Martin Gröschl from the Institute of Applied Physics at the Vienna University of Technology, who introduced me to the colleagues at the Medical University of Vienna, giving me the opportunity to work there. At this point, I want to thank all my colleagues who have supported me, especially Richard Haindl for investing so much time and interest. Thanks to Stanislava Fialová, who provided me with important reference images. I want to thank all the colleagues at the Center for Medical Physics and Biomedical Engineering for spreading such a good working atmosphere. Finally I want to acknowledge the Austrian Science Fund (FWF project P22329- N20) for the financial support.

Abstract

Optical Coherence Tomography (OCT) is an in vivo imaging technique which is able to perform tomographic or crosssectional images of biological tissues. It's main field of application lies in ophthalmology for acquiring 3D volumes of the retina. Thereby unique information about macular diseases such as diabetic retinopathy, or age related macular degeneration can be obtained. However, image contrast may be rather poor in conventional OCT imaging which can be overcome using polarization sensitive OCT (PS-OCT). Another limitation of state of the art is the limited transverse resolution of OCT instruments. The resolution can be improved using adaptive optics.

In this thesis an existing adaptive optics-scanning laser ophthalmoscope (AO-SLO) in combination with a time domain OCT (TD-OCT) was upgraded by an additional polarization sensitive channel in order to provide PS-OCT images with cellular resolution. PS-OCT improves the image contrast. Thereby additional information of the retina can be gathered, because several retinal structures (e.g. retinal pigment epithelium) change the polarization state of the light which can be detected using PS-OCT. Furthermore a dynamic focus scheme for achieving isotropic resolution through the whole volume OCT scan was calibrated. To improve the signal-to-noise ratio, the system was partially further developed. The new instrument was tested on technical samples as well as for in vivo retinal imaging. Representative images recorded in healthy volunteers are presented.

Kurzfassung

Die optische Kohärenztomographie (optical coherence tomography, OCT) ist eine in vivo-Bildgebungstechnik, die in der Lage ist, tomographische Querschnittsbilder des biologischen Gewebes aufzunehmen. In der Augenheilkunde wird es für die Aufnahme von 3D-Volumen der Netzhaut eingesetzt. Dabei können einzigartige Informationen über Makulaerkrankungen, wie diabetische Retinopathie oder altersbedingte Makuladegeneration erworben werden. Bei herkömmlichen OCT Systemen kann der Bildkontrast begrenzt sein, welcher durch ein polarisationsempfindliches OCT Systems verbessert werden kann. Eine weitere Einschränkung ist die beschränkte Querauflösung, die durch die Anwendung einer adaptiven Optik erhöht werden kann. In dieser Arbeit wurde ein vorhandenes Raster Scan laser Ophthalmoskop (adaptive optics-scanning laser ophthalmoscope, AO-SLO) in Kombination mit einem OCT durch einen zusätzlichen polarisationsempfindlichen Kanal erweitert. Dieses PS-OCT System soll die Detektion von polarisationsveränderten Licht ermöglichen. Dabei können zusätzliche Informationen von der Netzhaut erfasst werden, da mehrere Netzhautstrukturen (z.B. das retinale Pigmentepithel) den Polarisationszustand des Lichts verändern, was mit einem PS-OCT detektiert werden kann. Ferner wurde ein dynamisches Fokussystem zur Erzielung einer isotropen Auflösung über das gesamte Volumen kalibriert. Zusätzlich wurde das System teilweise weiterentwickelt um das Signal-Geräusch Verhältnis zu verbessern. Das neue Instrument wurde an technischen Proben als auch für in vivo Messungen getestet. Diesbezüglich wurden Messungen von gesunden Probanden aufgenommen und dargestellt.

Contents

1	Introduction and Motivation	5
1.1	Introduction	5
1.2	Anatomy of the Retina	6
1.3	Scope of Thesis	8
2	Fundamentals of OCT	9
2.1	Time domain OCT: Principle	9
2.1.1	Mach-Zehnder Interferometer	9
2.1.2	Interference of electromagnetic waves	10
2.1.3	Theory of Coherence	13
2.1.4	Dispersion Compensation in OCT	14
2.2	Polarization sensitive OCT: Principle	15
2.2.1	Birefringent material	17
2.3	PS-OCT: Principles	19
2.4	Adaptive Optics	21
2.4.1	Principle of Adaptive Optics	21
3	Method	23
3.1	Overview	23
3.2	AO-SLO - Sample Arm	23
3.2.1	Light source	25
3.2.2	Shack Hartmann Sensor	27
3.2.3	Deformable Mirror	27
3.2.4	Detection unit	28
3.3	PS-OCT configuration - Reference Arm	29
3.3.1	Cross Polarization Channel	31
3.4	System Performance	32
4	Results and Discussion	39
4.1	Calibration of the dynamic focus	39
4.1.1	Test resolution target measurements	41
4.2	In vivo measurements with dynamic focus	42

4.2.1	Intensity 3D OCT Imaging of human retina	42
4.3	Comparison between SLO and OCT images	44
4.4	Polarisation sensitive images	46
4.4.1	Image of a birefringent test sample	46
4.4.2	PS-OCT of the human retina	48
5	Conclusion	50

1 Introduction and Motivation

1.1 Introduction

Optical Coherence Tomography (OCT) is an in vivo imaging technique which is able to perform tomographic or crosssectional images of biological tissues [1] [2]. It is working similar to an ultrasound instrument but instead of using sound waves it operates with near infrared, low coherence light for achieving high resolution images of three dimensional volumes in real time. OCT can be used for acquiring a 3D volume of the retina (posterior segment of the eye) in order to get information of its structure. With this method images of macular diseases such as diabetic retinopathy, age related macular degeneration, macular holes, epiretinal membranes can be recorded which greatly improves diagnosis compared to conventional methods. Although the axial resolution of OCT lies in the order of a few μm , the transverse resolution remains limited. Thereby imperfections of the eye optics introduce aberrations to the imaging beam which prevents imaging with higher resolution. An improvement of transverse resolution can be achieved with adaptive optics which corrects for monochromatic aberration [3]. Normally adaptive optics is often used in combination with a Fourier-domain optical coherence tomography (FD-OCT) system, which records simultaneously the whole imaging depth leading to a better sensitivity compared to a previously used time domain technique [4][5]. However, using AO results in a limited depth of focus ($<100\mu\text{m}$). Since the retina has an depth extension of $500\mu\text{m}$ only part of the 3D volume will be in focus and imaged sharply. An alternative approach for high transverse resolution imaging might be transversal scanning OCT [6] [7]. With this technology isotropic resolution through the entire volume can be achieved using a dynamic focus scheme. Thereby, the coherence gate in z-direction is simultaneously shifted with the focal plane. One drawback of TS-OCT is the sensitivity to axial eye motion. However, this can be overcome through the implementation of an axial eye tracker, which is capable of correcting the axial eye motions in real time [8] [9]. Recently, an instrument has been introduced that provides high lateral and axial resolution images with a high signal to noise ratio (SNR) in SLO and OCT [10]. However even with this setting the identification of the retinal pigment epithelium layer (RPE) is quite delicate. Earlier works showed that the RPE has a depolarizing character [11]. In order to enable the detection of the depolarizing effect and to provide an unique ability to reliably detect the location of the RPE, polarization sensitive OCT has to be employed. In this thesis an existing AO-SLO/OCT system [10] was upgraded with an additional polarization sensitive channel in order to provide PS-OCT images with

cellular resolution. In previous work polarization sensitivity was implemented in an AO-FD-OCT system [12]. However, the transverse imaging speed of that system was limited and no en-face images of retinal tissue could be provided.

1.2 Anatomy of the Retina

Figure 1 shows a schematic diagram of the retina.

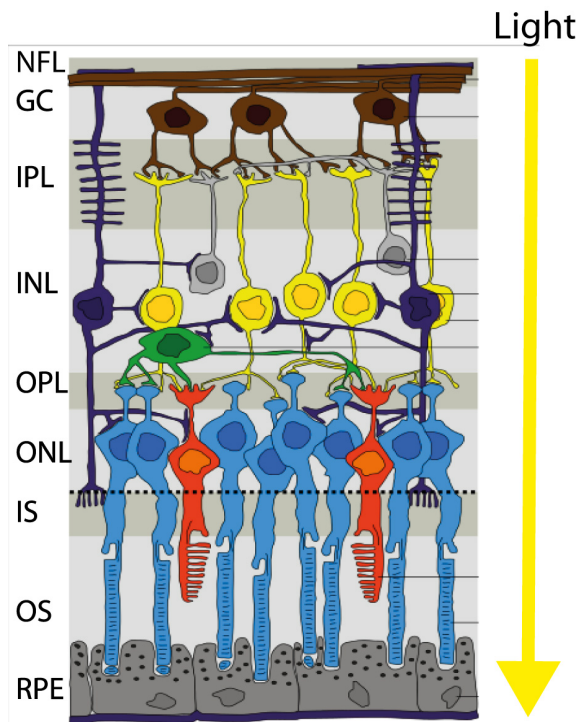


Figure 1: Schematic Diagram of the histological layers of the retina. From top to bottom: Nerve fibre layer (NFL), Ganglion cell layer (GC), Inner plexiform layer (IPL), Inner nuclear layer (INL), Outer plexiform layer (OPL), Outer nuclear layer ONL, Outer limiting membrane (OLM), Inner segment of photoreceptor (IS), Outer segment of photoreceptor layer (OS), Retinal pigment epithelium (RPE). [13]

Before being detected by the photoreceptors (rods and cones) the light has to traverse several retinal layers. The layer of rods and cones is subdivided into the inner (IS) and the outer segmented(OS) layer [13]. In intensity based OCT images (Figure 2) the different layers of the retina can be easily differentiated. However, the separation between the end tips of photoreceptors (ETP) and RPE is not pronounced and these layers are difficult to distinguish. The RPE plays a fundamental role in retinal diseases such as AMD and has many functions like the storage and enzymatic conversion of vitamin A or the absorption of light for the melanin synthesis. Therefore, the clear identification of this layer is highly important [14]. PS-OCT exploits the polarization properties of light and can be used to determine the exact

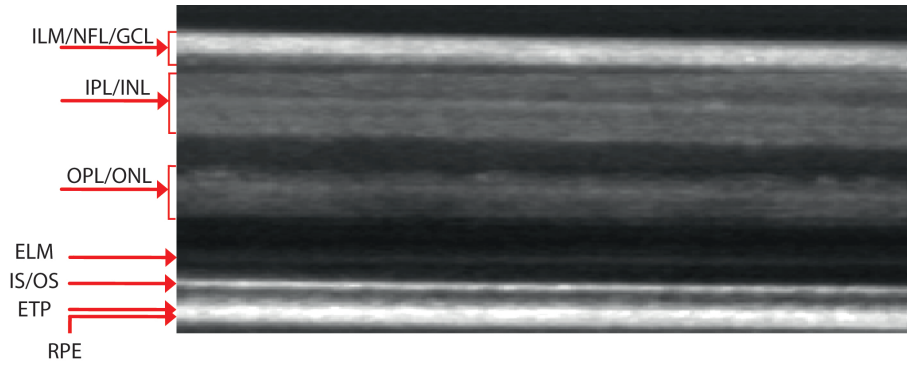


Figure 2: Averaged OCT B-scan of the retina in a healthy volunteer recorded with the AO-SLO/OCT system ($500\mu\text{m}$ in depth, 1° lateral extension). ETP...End tips of the cone photoreceptors. (The separation between ETP and RPE is hardly visible), Arrow shows the incident light

location of the RPE based on its depolarizing character [11]. Besides the depolarizing RPE additional structures of the retina change the polarization state of the light and PS-OCT can be used to provide increased contrast [15] [16]. In this context the retinal nerve fiber layer (RNFL) and Henle's fiber layer have to be mentioned. Both structures are birefringent because of the regular arrangement of the fibrils. This birefringence causes a delay (retardation) between two orthogonal polarization components which can be measured using PS-OCT [17] [18].

1.3 Scope of Thesis

This thesis focuses on the development of a polarization sensitive time domain (en-face) OCT for in vivo measurement of the human retina. Thereby a previously developed AO enhanced SLO/OCT instrument [10] was upgraded. Remarkable polarization sensitive images were already achieved with spectral/Fourier domain OCT [17] [18]. However the transversal resolution in these systems is quite limited. One system was combined with AO [12], however, it was too slow to provide en-face images with sufficient quality. With the implementation of PS-OCT we want to enhance the image contrast compared to conventional intensity based imaging. One specific imaging target of the combination with AO is the visualization of individual RPE cells. These can currently not be clearly resolved using intensity based OCT [10]. Another application might be the quantification of birefringence introduced by single nerve fiber bundles.

The thesis is organized as follows: Chapter 2 discusses the theory and principle of time domain optical coherence tomography just as well as the principle of adaptive optics. Thereby the influence of dispersion, polarisation and the corresponding theoretical background theory are described.

Chapter 3 focuses on the development and characterization of the PS-OCT system. The sample arm, reference arm, the eye tracking system and their assembly are presented shortly. The performance of the system which is also specified in this chapter.

Chapter 4 presents the results of the polarization sensitive TD-OCT instrument in combination with an AO-SLO and an eye tracking system. Using dynamic focusing high resolution retinal images extracted from 3D volumes are displayed.

Chapter 5 treats the conclusion and outlook.

2 Fundamentals of OCT

Optical coherence tomography is an interferometric imaging technique [1] [2]. Meanwhile widespread applications of this technique can be found ranging from biomedical imaging (such as retinal imaging, anterior segment imaging, endoscopic imaging, cardiovascular imaging) to non destructive imaging and testing in material sciences. It is a non contact and non destructive method for gaining two and three dimensional images of tissues [19]. The difference to conventional microscopy is that in addition to the surface information OCT can also obtain information from the deeper layers [20]. Doing so a common OCT is working by superposing two light beams. This two beam interference is described in following section 2.1. Advanced modification like the PS-OCT will be described in section 2.2 and 2.3. Improvements in lateral and transversal resolution can be achieved by using adaptive optics and dynamic focus which is explained in section 2.4.

2.1 Time domain OCT: Principle

OCT is based on low-coherence interferometry. This low coherence property allows to record images in a depth resolved way. Thereby the intensity of the backscattered light gets coherently amplified which enables the detection of weak signals [19]. There are several variations of interferometer types. The system used in this thesis is based on a Mach-Zehnder interferometer and will be explained in the following.

2.1.1 Mach-Zehnder Interferometer

Figure 3 shows a scheme of a Mach-Zehnder interferometer. An optical source illuminates the interferometer. Frequently, a superluminescent diode (SLD) is used for this purpose. A SLD emits light with a broad spectrum which results in a short coherence length. The light gets divided by a beam splitter into the reference and sample beam. If both beams have exactly the same path length, interference fringes can be observed that can be recorded by a photodetector. Travelling through a sample, with the refractive index n , the velocity of light v_0 gets changed by $v_0 = n \cdot c_n$. Because a short coherence light source is used, an interference signal can only be detected if the optical path difference between reference and sample arm light is lower than the coherence length l_c . In case of being larger, the translation stage (TS) in the reference arm can be adjusted to match the length of the sample arm path. l_c is an important quantity for a good axial resolution, which depends inversely on the spectral width Δk of the light source $l_c \propto 1/\Delta k$. A typical OCT works with

a broad spectrum in order to get a low coherence length (which is in the order of some micrometer), which is equivalent to an high axial resolution. By moving the translation stage TS, it is possible to get depth-resolved images [19].

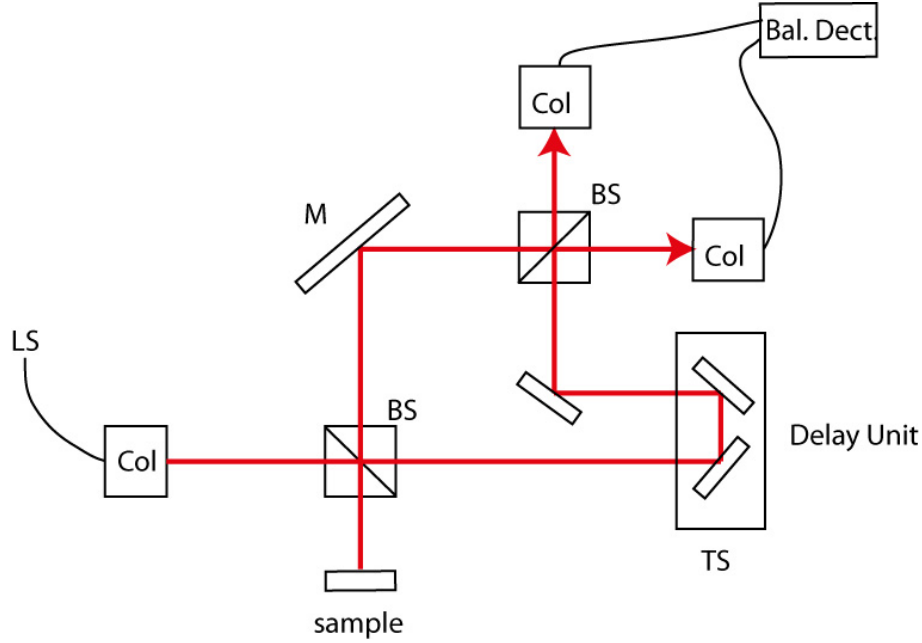


Figure 3: Scheme of a Mach Zehnder interferometer for OCT applications: LS...Light Source, BS...Beam Splitter, Delay Unit with a phase shift of $\Delta\phi$ Col...Collimator, Dect...Detector, M...Mirror, delay unit consisting of two mirrors that are mounted on a translation stage (TS).

2.1.2 Interference of electromagnetic waves

Electromagnetic wave

In order to understand interference it is important how light is defined. Light is an electromagnetic wave and its characteristic is described by Maxwell's equations. It consists out of two vector fields, the electric vector field \vec{E} and the magnetic vector field \vec{H} . One solution of Maxwell's equations are plane waves that can be expressed as [21]

$$\vec{E} = \vec{E}_0 \cos(\vec{k}\vec{x} - \omega t) \quad (2.1)$$

$$\vec{B} = \vec{B}_0 \cos(\vec{k}\vec{x} - \omega t) \quad (2.2)$$

where \vec{k} is the direction of propagation of the plane wave, \vec{x} the location in space and ω the phase of the wave. The electric and magnetic fields are orthogonal to each other and are illustrated in Fig.4. An electromagnetic wave has polarization characteristics as will be discussed later.

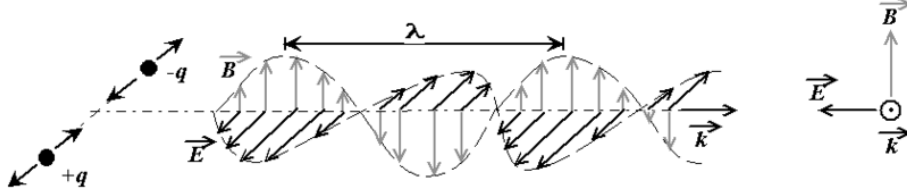


Figure 4: Illustration of an electromagnetic wave: The wave is defined by a magnetic field (\vec{B}) and an electric field (\vec{E}) that is orthogonal to \vec{B} and to \vec{k} . \vec{k} represents the vector of the propagation direction. λ is the wavelength and q is the direction of oscillation of the charge carrier. [22]

Interference

In the following the magnetic field component will be neglected. For simplicity we take two waves with the same frequency and propagation speed which can be written as

$$E_1(x, t) = E_{01} \sin[\omega t - (kx_1 + \epsilon_1)] \quad (2.3)$$

$$E_2(x, t) = E_{02} \sin[\omega t - (kx_2 + \epsilon_2)] \quad (2.4)$$

in which E_1 and E_2 are the amplitudes and ϵ_1 and ϵ_2 are the space parts of the phase. A linear superposition of equation 2.3 and 2.4 equals an interference of the two waves and the resulting total field can be expressed as

$$E_{total} = E_1 + E_2 \quad (2.5)$$

It is to be seen that the most crucial factor is the phase difference δ of the phases ϵ_1 and ϵ_2 . Depending on δ the resultant amplitude is increasing or decreasing as can be seen in Fig. 5. Forming δ out of equation 2.3 and 2.4 we get

$$\delta = (kx_1 + \epsilon_1) - (kx_2 + \epsilon_2) \quad (2.6)$$

Phase differences of $0, \pm 2\pi, \pm 4\pi..$ lead to a maximum amplitude (constructive interference), in case of $\delta = \pm\pi, \pm 3\pi, \dots$ the amplitude is a minimum (destructive interference). [21]

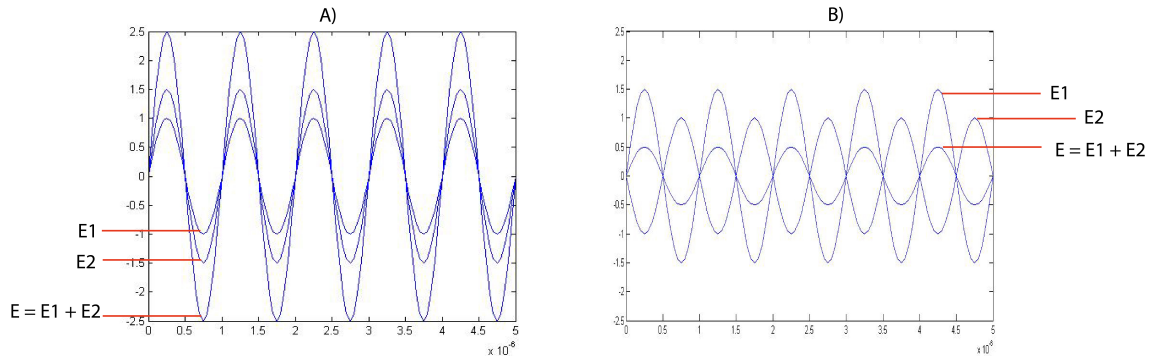


Figure 5: Superposition of two waves (E1 and E2) with the same frequency but a different amplitude: A) phase difference = 0; B) phase difference = π

One of the easiest ways to show interferences is the double slit experiment or Young's Experiment, illustrated in Fig. 6. Thereby a plane wave gets diffracted by two slits and is brought to interference afterwards.

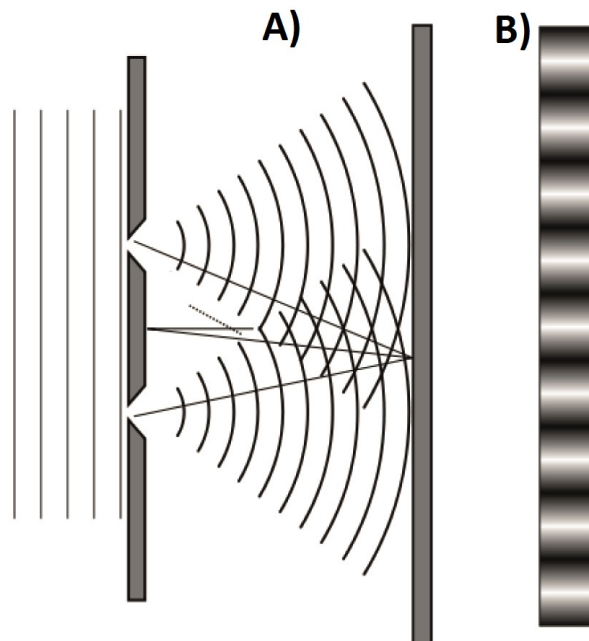


Figure 6: Illustration of Young's double slit experiment which leads to an inference of two identical spherical waves. A) Propagation of the plane wave through the double slit. B) Corresponding interference pattern observed in the imaging plane.

[23]

This leads to a typical interference pattern as is shown in Fig. 6B). In the case of an

OCT system (cf. Fig. 3) the intensity at the interferometer exit can be calculated by

$$I = \frac{n}{2\mu_0 c} (E_{s0}^2 + E_{r0}^2 + \sqrt{E_{s0} E_{r0}} \cos(kz_3 - kz_s)) \quad (2.7)$$

where E_{s0} is the returning wave from the sample arm and E_{r0} is the field amplitude of the light returning from the reference arm, $z_r - z_s$ is the path length difference between reference and sample arm, μ_0 the magnetic permeability and c the speed of light in vacuum. The last term of Eq. 2.7 corresponds to the so called interference term. With the sample intensity and the reference intensity, the detected intensity I in equation 2.7 can be calculated.

2.1.3 Theory of Coherence

Understanding coherence is essential for optical coherence tomography. In order to determine the axial location within a sample where light is backscattered OCT has to use low coherence light. The coherence time is defined by the spectral bandwidth Δf of the light source and can be expressed as [24]

$$t_c \sim \frac{1}{\Delta f} \quad (2.8)$$

Expressing the spectral bandwidth of the light source through the corresponding wavelength, the coherence time becomes

$$t_c \sim \frac{1}{c} \cdot \frac{\lambda_0^2}{\Delta \lambda} \quad (2.9)$$

or if we introduce the coherence length

$$l_c \sim \frac{\lambda_0^2}{\Delta \lambda} \quad (2.10)$$

In case of being a Gaussian emission spectrum $E(\lambda) \propto e^{-4 \ln 2 \left(\frac{\lambda - \lambda_0}{\Delta \lambda} \right)^2}$, the coherence length is defined as

$$l_c = \frac{4ln2}{\pi} \frac{\lambda_0^2}{\Delta\lambda} \quad (2.11)$$

We can see in equation 2.11 that the coherence length depends on the central wavelength λ_0 and the spectral width $\Delta\lambda$. The axial resolution Δz in OCT (cf. 2.12) is defined as half of the coherence length because of the double pass configuration in OCT systems (the light goes the same way twice, cf. Fig. 3)

$$\Delta z = \frac{2ln2}{\pi} \frac{\lambda_0^2}{\Delta\lambda} \quad (2.12)$$

The typical central wavelength in OCT for retinal imaging is around 840nm. The standard bandwidth of the SLD's in this wavelength region is ~ 50 nm which results in an axial resolution of these systems of $6.2\mu\text{m}$ in air. In tissue the axial resolution is improved by a factor corresponding to the refractive index of the tissue. Assuming a refractive index of 1.4 in the retina, the typical OCT axial resolution will be $\sim 4.5\mu\text{m}$.

2.1.4 Dispersion Compensation in OCT

Dispersion mismatch between the two interferometer arms results in a degradation of the axial resolution [25]. Dispersion is caused by the wavelength dependence of the refractive index which results in different optical path lengths for each wavelength. In order to overcome effects caused by dispersion, both interferometer arms have to be optically matched. Ideally, the same optical components (lenses, fibers) are used in both interferometer arms to compensate for dispersion.

2.2 Polarization sensitive OCT: Principle

This section will introduce the principle of polarization sensitive OCTs (PS-OCT). Common OCTs are in general polarization insensitive and have therefore limited image contrast. In the following the underlying principles of PS-OCT are explored. Polarization effects are caused by anisotropy of optical media that are traversed by light. Without losing generality, each field vector can be composed of two orthogonal field vectors. The horizontal \vec{E}_h and the vertical field \vec{E}_v of this vector can be written as

$$\vec{E}_h(z, t) = iE_{0x} \cos(kz - \omega t) \quad (2.13)$$

and

$$\vec{E}_v(z, t) = jE_{0y} \cos(kz - \omega t + \epsilon) \quad (2.14)$$

Thereby ϵ is the phase difference between both vector fields. The summation of these two vector fields results in the electric vector \vec{E} [21].

$$\vec{E}(z, t) = \vec{E}_h(z, t) + \vec{E}_v(z, t) \quad (2.15)$$

or in case of ϵ being 0,

$$E(z, t) = (iE_{0x} + jE_{0y}) \cos(kz - \omega t) \quad (2.16)$$

Depending on this value \vec{E}_v lags \vec{E}_x by $\epsilon > 0$ or leads by $\epsilon < 0$. If $\epsilon = 0, \pm 2\pi, \dots$ both cosine functions in equation 2.15 and 2.14 have the same values and the waves are in phase.

Linear Polarisation

Fig. 7A) shows a scheme of a linear polarized light field. Looking just at the x-y plane we get following scheme (Fig. 8). In a linear polarized state the electric field oscillates within a fixed plane spanned by the propagation vector and the electric field vector. [21].

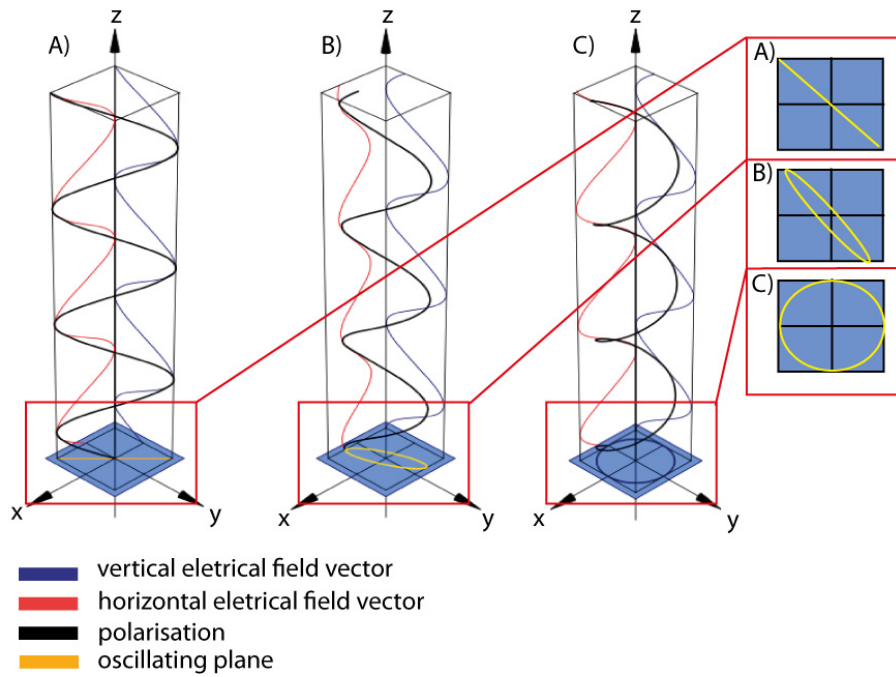


Figure 7: Scheme of polarization states. A) linear polarization B) elliptical polarization C) circular polarization. [26]

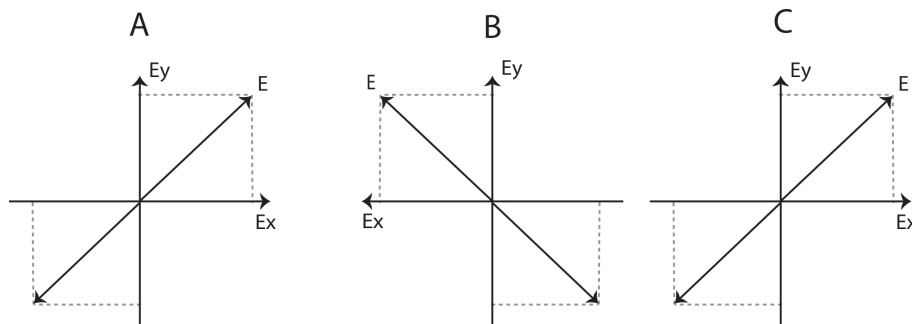


Figure 8: A($\epsilon = 0$) and C($\epsilon = \pm 2\pi$) oscillating in the first and third quadrant and B($\epsilon = \pm \pi$) oscillating in the second and fourth quadrant

Circular and elliptic polarization states

In the case that the phase difference between horizontal and vertical components is $\epsilon \neq 0, \pm\pi, \pm 2\pi, \dots$ the polarization state will be circular (cf. Fig. 7B)) or elliptical (cf. Fig. 7C)). Thereby the resulting field vector \vec{E} is rotating at an angular frequency of ω along the z-axis.

Depending on the leading sign of the phase difference of ϵ the electric field vector is rotating clockwise or counter-clockwise (Fig. 9) around the axis of light propagation.

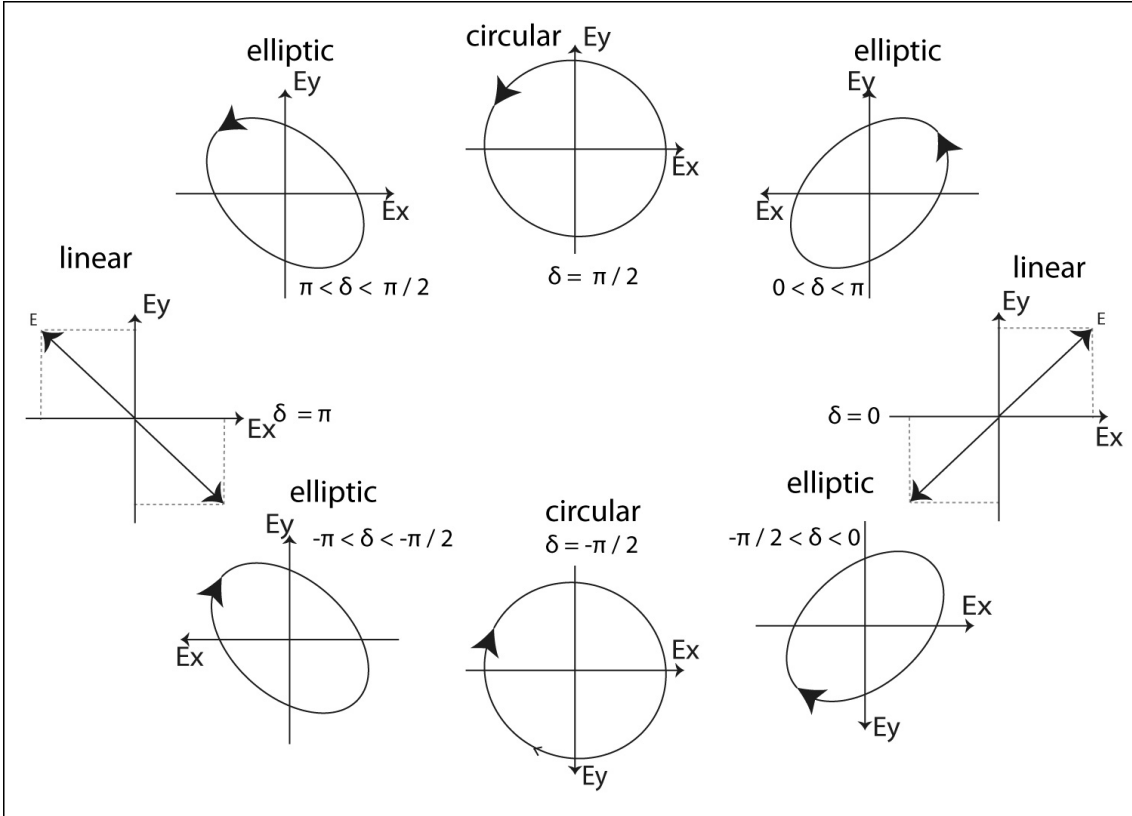


Figure 9: Scheme of different polarisation states with rotating directions that are dependent on the phase difference between the two orthogonal electric field vectors ϵ : Linear, elliptic and circular polarisation.

2.2.1 Birefringent material

Birefringent material has the ability to delay the phase between horizontal and vertical electric fields. Thereby the refractive index of the material depends on the orientation of the electric field vector which is leading to the phase shift between the fields. Such a phase shift is called retardation and results in a change of the

polarization state, mostly into an elliptical state and can be detected using PS-OCT. Due to the birefringence, two different optical axis can be determined within the material along, which different propagation velocities can be observed. The fast axis (where the refractive index is lower) and the slow axis (where the refractive index is larger).

2.3 PS-OCT: Principles

There have been a variety of different techniques to achieve polarization sensitive OCT. These mainly differ in the number of polarization input states that have to be used to obtain the PS-OCT data. In this thesis the single input state method is used. A scheme of the principle setup is shown in Fig. 10 [27] [28] [29]. The key features of the system are a polarization sensitive detection unit and that the sample is illuminated with circular polarized light. More details on such a system can be found in [27] [28].

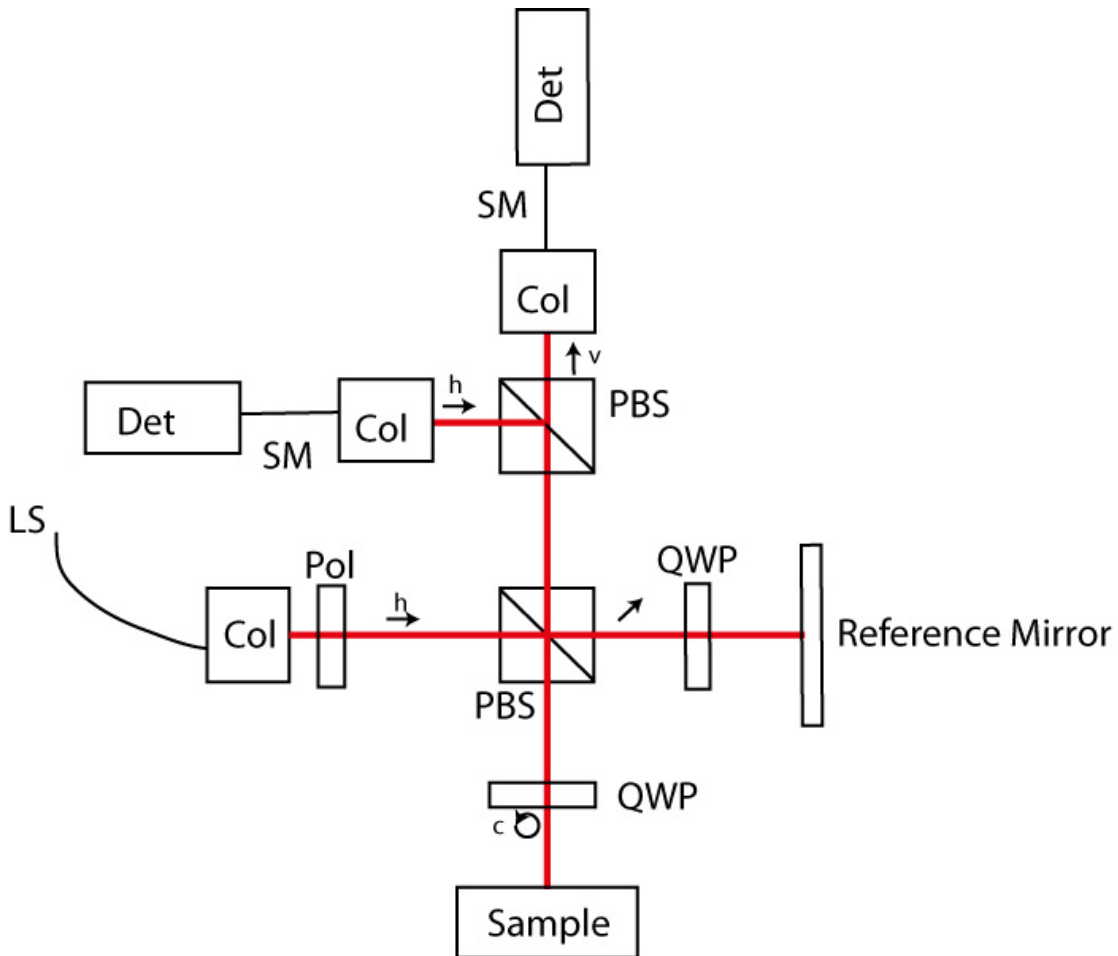


Figure 10: Scheme of a PS-OCT system: LS...light source, P...polarizer, PBS...polarizing beam splitter, QWP...quarter wave plate, Col...Collimator, Det...Detector, v... vertical polarization state, h...horizontal polarization state, SM...single mode fiber

From the recorded data several parameter can be calculated. In this thesis following parameter are used: reflectivity, retardation and optical axis orientation.

Calculation of polarization sensitive parameter.

PS-OCT is able to record the interference signal of the horizontal and vertical polarization state:

$$\tilde{A}_{H,V}(Z) = A_{H,V}(z) \exp[i\phi_{H,V}(z)] \quad (2.17)$$

where A is the amplitude of the interference signal, z the depth coordinate and ϕ the phase of the signal [27]. The reflectivity image R is represented by the sum of the intensity signal A_H and A_V :

$$R(z) \propto [A_H(z)]^2 + [A_V(z)]^2 \quad (2.18)$$

This image corresponds to OCT images recorded with a polarization in-sensitive system.

If light encounters a birefringent material a phase shift between the horizontal and vertical polarization state occur. Such a phase shift can be calculated via:

$$\delta(z) = \arctan \left[\frac{A_V(z)}{A_H(z)} \right] \quad (2.19)$$

where δ is the phase (retardation) and A_V and A_H are the measured amplitudes of the horizontal and vertical channel, respectively.

The optical axis is encoded in the phase difference between the two channels [28],

$$\theta = \frac{180 - \Delta\Phi}{2} \quad (2.20)$$

where $\Delta\phi$ is the phase difference of the received signals and θ the optical fast axis orientation of the birefringent sample.

2.4 Adaptive Optics

Adaptive optics (AO) is used for correcting wave front distortions. It is required for optical setups with high aberrations, such as in astronomy for ground based telescopes. Due to different refraction indices of the air layers in the atmosphere, the wave front gets distorted leading to unsharp images. In order to correct such deformations of the wave front, an adaptive optics setup can be used in the telescope leading to diffraction limited images of the sky [30]. Imperfections in the optics of the eye lead to similar wavefront distortions and finally to a degradation of the image quality achieved in the retina that can be obtained with optical instruments. In order to overcome this limitation AO can be used to correct for these distortions yielding diffraction limited imaging performance in the living human eye [31].

2.4.1 Principle of Adaptive Optics

A basic scheme of an adaptive optic setting is shown in Fig. 11. Wave front distortions are detected by a wave front sensor (WFS). The AO software calculates from the measured wavefront distortions corresponding voltage values for each actuator of the deformable mirror in order to change the shape of the mirror. Usually, the DM has a reflecting membrane which shape can be changed by shifting by several actuators, that are located behind the membrane. The DM can take various shapes because each actuator can be controlled independently. Normally the adaptive optics correction is working in closed loop mode which means that the wavefront is measured again after the shape of the mirror had been changed and new voltage values (corresponding to the residual wavefront distortions) are send to the DM. Thereby, the wavefront distortions are iteratively minimized until diffraction limited performance is achieved.

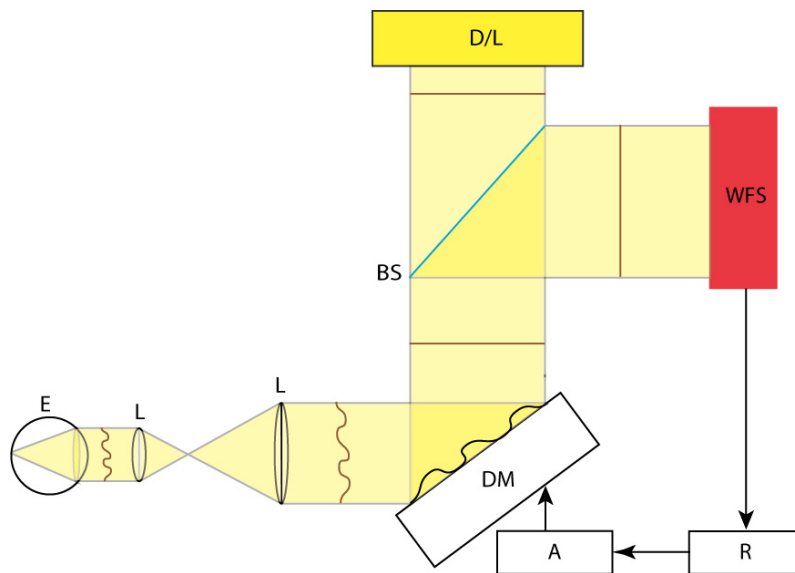


Figure 11: Scheme of an adaptive optics system for ophthalmology. E...Eye, L...Lenses, DM...deformable mirror, BS...Beam splitter, D/L...Detector/Light source, WFS...Wave front sensor, R...Reconstructor, A...Actuator controller

3 Method

In this section the used AO-SLO/OCT system will be described and the design of the polarization sensitive OCT system is introduced. Problems that occurred during the implementation of the PS-OCT setup are addressed. Finally, the performance of the system is assessed.

3.1 Overview

In order to perform polarization sensitive OCT measurements the AO-SLO/OCT system introduced by F. Felberer et al. [10] had to be modified. The whole system is based on a Mach-Zehnder interferometer. The original setup consists of 3 parts: the AO-SLO/OCT sample arm, the reference arm and an axial eye tracking system. Note that the original system is already polarization sensitive. This was necessary in order to minimize influences of backreflections at the lenses on the wavefront measurements. However, only the co-polarized OCT channel was recorded and the light returning to the cross-polarized channel was not used.

3.2 AO-SLO - Sample Arm

A scheme of the sample arm is shown in Fig. 12.

The light source (LS), the Shack Hartmann sensor (SH-sensor) and the DM are here the most crucial components and will be described in following subsections. More detailed information on the setup can be found in the publication of Felberer et al.[32], since the same sample arm configuration is used. In short, the system is based on lenses instead of spherical mirrors (cf. Fig.12). Raster scanning of the retina is performed by a Galvo scanner (GS) and a resonant scanner (RS) which is operating at 8kHz. The AO system consists of a DM (Imagine Eyes, mirao 52-e), a Shack Hartmann wavefront sensor (SHS, Imagine Eyes, Haso 32) and the corresponding AO-software (Casao, Imagine Eyes). One drawback of the lens system are back-reflections occurring at the lens surfaces which influence the wavefront measurements. These reflections can be suppressed by polarization optics. After collimation of the beam the light is linear polarized and traverses all optical components. Before entering the eye, the light has to traverse a quarter wave plate (QWP) which is oriented at 45° in respect to the incident linear polarization state. Thereby the light will be in a circular polarization state. Figure 13 illustrates the different polarization states before and after the QWP. If the sample introduces no polarization change, the phase of the backscattered light gets shifted by 90° after

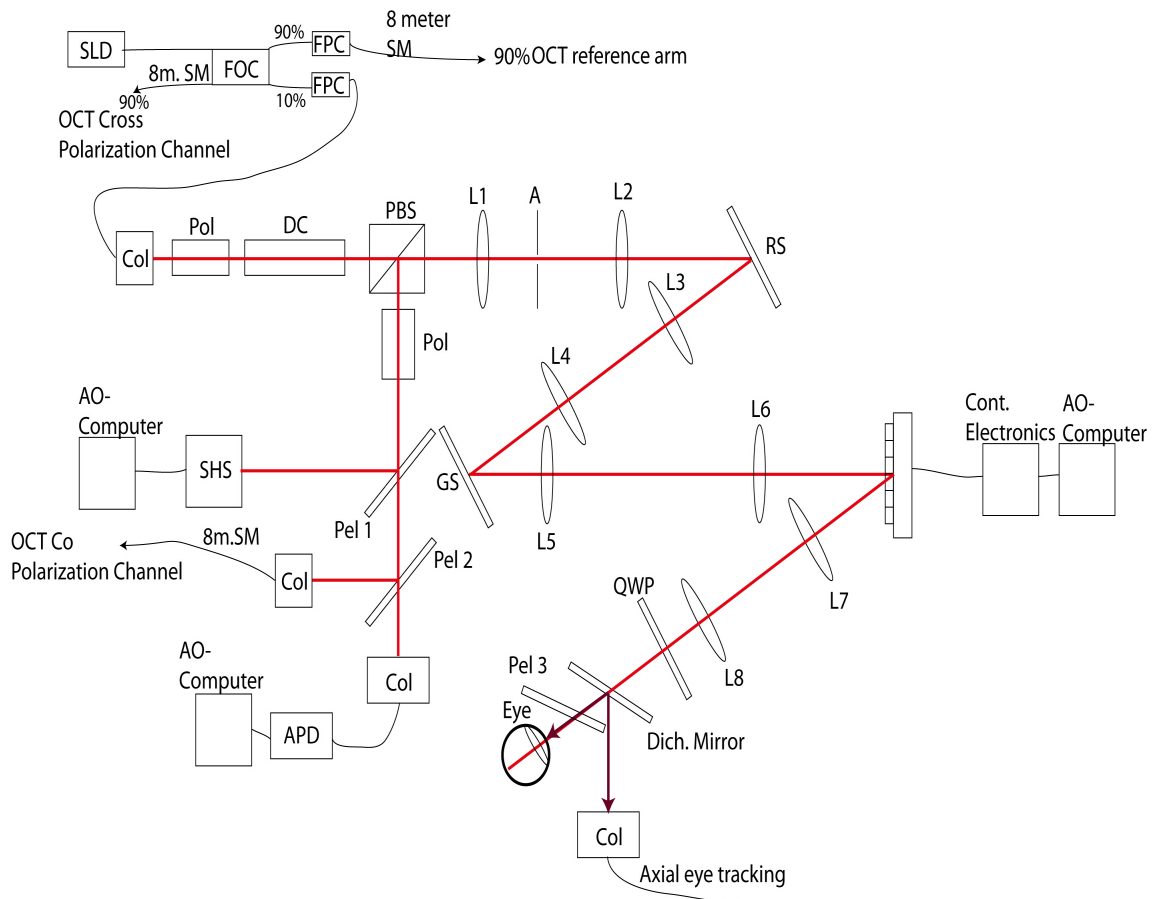


Figure 12: Scheme of the sample arm. SLD...Super luminescent diode(light source), FOC...fiber optic coupler (90:10), FPC...Fiber polarization controller, L...Lenses, RS...Resonant scanner, GS...Galvanometer scanner, DM...Deformable mirror, QWP...Quarter wave plate, Col...Collimator, SHS...Shack Hartmann sensor, APD...Avalanche photo diode, Pel...Pellicle, SM...single mode fiber, Pol...Polarizer, DC...Dispersion compensation. Adopted of [10]

traversing the QWP a second time, leading once again to a linear polarisation state which is orthogonal to the incident polarization state. In order to properly align the orientation of the QWP a polarizer (analysator) was placed after the QWP and the outgoing light power was measured with a power meter (at the location of the eye). In the case of circular polarized light, the measured power has to be independent on the orientation of the polarizer. On the way back, the light gets split into 4 channels whereby the co-polarized light gets divided into the SHS (20%), the SLO detection channel (20%) and the OCT co-polarized detection channel (60%). The cross-polarized OCT detection channel receives 90% of the cross polarized light (10% is directed to the light source because of the 90:10 fiber coupler at the interferometer entrance).

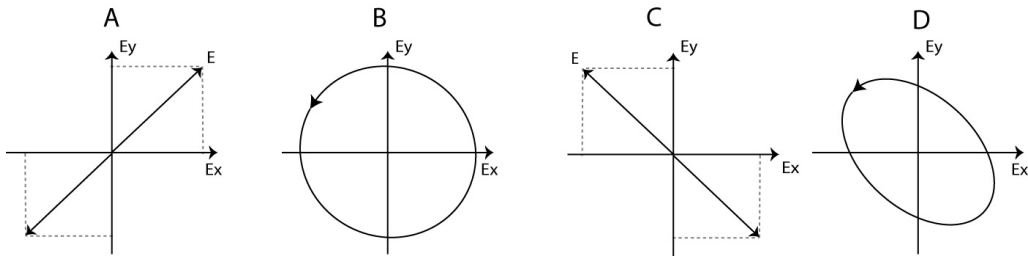


Figure 13: Different polarization states of the light before and after traversing the QWP in the sample arm of the AO-SLO/OCT system: A: linear polarization state before qwp; B: circular polarization state after qwp; C: linear polarization state if sample has no influence on the polarization state; D: elliptical polarization state in case of an birefringent sample

One problem for PS-OCT measurements was the pellicle ($T=92\%$, $R=8\%$) in Fig. 12, which was responsible for coupling the fixation target into the instrument. Depending on the orientation of the pellicle, diattenuation is introduced which would influence the PS-OCT measurements. Therefore the pellicle was removed from the system. In the following different components of the sample arm are explained in more detail.

3.2.1 Light source

The system uses a superluminescent diode (SLD) by Superlum with a central wavelength of 840nm and a spectral bandwidth of 50nm. Figure 14 shows the emission spectrum of the light source and the main characteristics of the SLD are given in Table 1.

Using light in the near infrared has many advantages. Since energy is defined by $E = hf$ and $f = \frac{c}{\lambda}$, the allowed light exposure level on the retina, as given in the laser safety regulations [33], can be higher at longer wavelengths. Furthermore the

Table 1: Characteristics of the used light source

Central Wavelength [nm]	840
Spectral bandwidth [nm]	50
Output Power [mW]	25.9

penetration of light is increased with longer wavelengths because scattering in tissue is reduced.

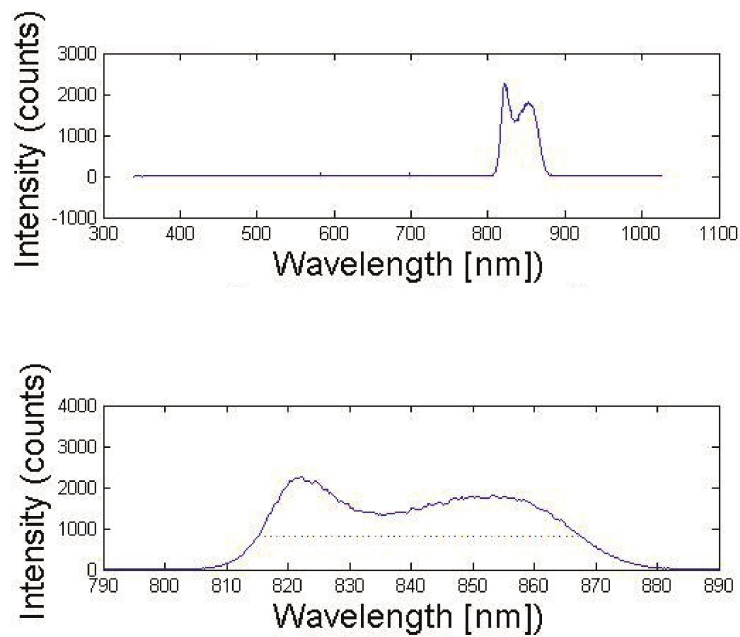


Figure 14: Emission spectrum of the used light (a SLD) source with a center wavelength of 840nm and a bandwidth of 50nm measured with a commercial spectrometer (Ocean Optics USB 2000)

3.2.2 Shack Hartmann Sensor

The wave front detection is done by a Shack Hartmann sensor (Haso 32, Imagine Eyes, Orsay, France), which has 1280 lenslets to sample the wavefront exiting the eye. The accuracy of the wave front deformation depends on the number of lenslets. However, with increasing number of lenslets the received light per location is decreasing, which results in a higher exposure time. Since for in vivo adaptive optics measurement a low exposure time (about 20ms in in vivo measurements) is needed, the number of lenslets is limited. The wavefront reconstruction and the calculation of the proper voltage values for the DM is done by the CASAO software that is provided by the manufacturer of the SH sensor and the DM. [34]

3.2.3 Deformable Mirror

The correction of wave front deformations is done by the DM (Mirao 52, Imagine Eyes, Orsay, France) with 52 actuators. The mirror supports high strokes and is able to correct defocus and astigmatism up to 50 μm . More characteristics are shown in Table 2 [34].

Table 2: Characteristics of deformable mirror: Mirao 52, Imagine Eyes, Orsay, France [34]

Actuators	52
Effective pupil diameter	15 mm
Maximum generated wavefront	$\pm 50 \mu\text{m}$
Surface quality	0.01 μm
Wavefront quality	0.02 μm

With this mirror it is possible to set the focus in the retina in individual layers and to change the focus dynamically during measurements. During a volume scan with TS-OCT the coherence gate is continuously shifted with a given range in z-direction. Using AO the depth of focus is $<100\mu\text{m}$ which causes part of the imaged volume to be unsharp (out of focus). To overcome this limitation, the shape of the DM can be changed during the measurement leading to a dynamic shift of focus simultaneously to the coherence gate. This yields isotropic resolution throughout the imaging depth. Fig. 15A shows the beginning of a 3D volume measurement and B the change of the DM which results in a shift of the focal plane.

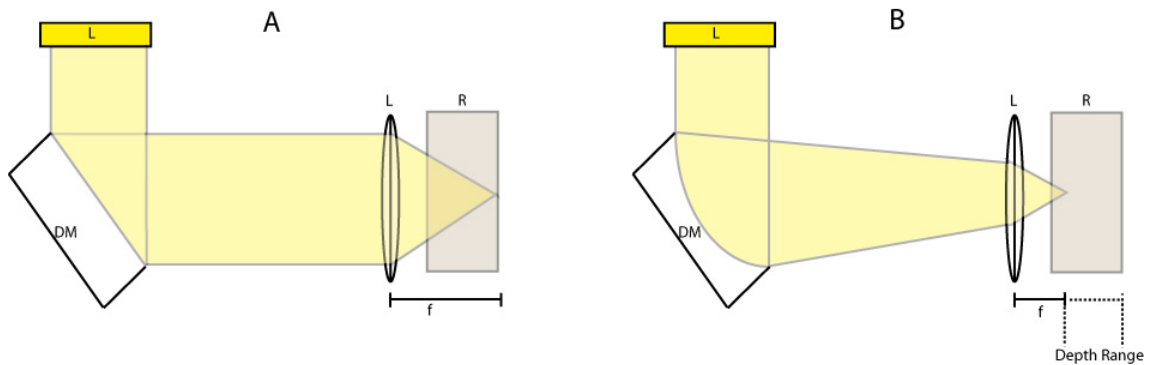


Figure 15: Illustration of changing the focus with a deformable mirror. L...Light source, DM...Deformable mirror, L...Lens, R...Resolution target. A) Starting focus, B) Defocus caused by a change of the DM

3.2.4 Detection unit

The detection unit consists of an APD for the SLO channel and two 8 meter long single mode fibers that are used to direct the light to the final fiber optic beam splitter of the Mach Zehnder interferometer. There the light is brought to interference with the light returning from the reference arm.

3.3 PS-OCT configuration - Reference Arm

The main modification (compared to the setup presented in [10]) for PS-OCT had to be done in the reference arm of the interferometer. A scheme of the new reference arm is presented in Fig. 16. The main change has been done for the detection unit that now consists of two channels (for the co- and cross-polarized light).

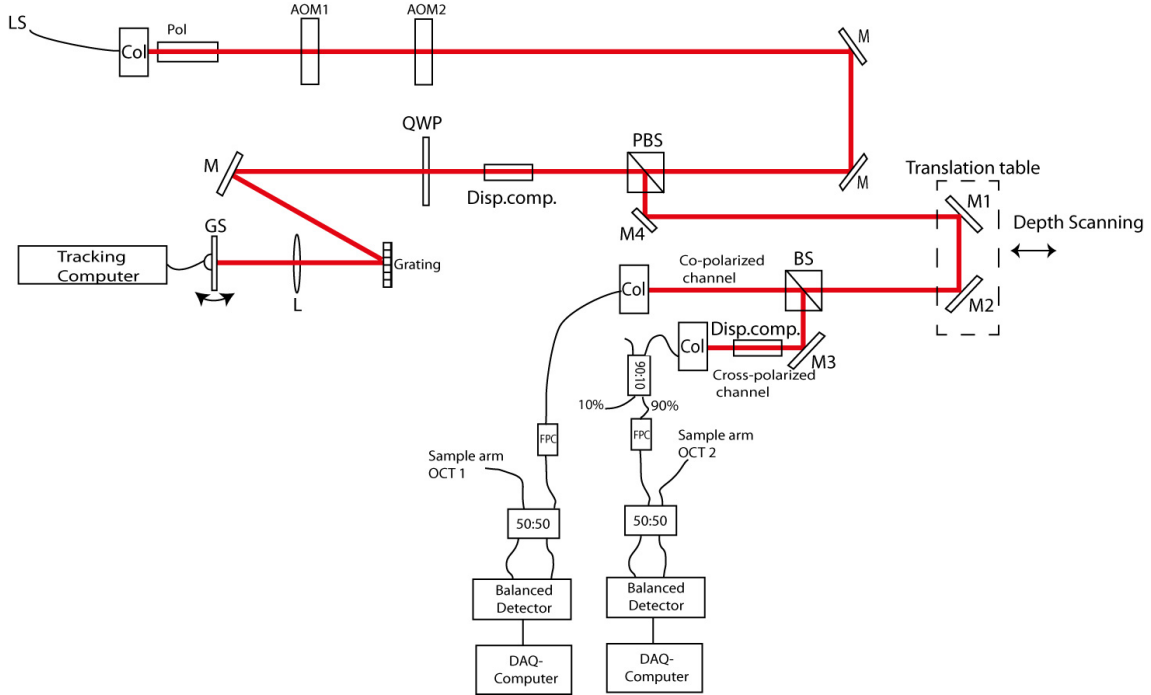


Figure 16: Scheme of the reference arm with two OCT channels for polarization sensitive data acquisition. LS...Light source, Pol..Polarizer, AOM... Acousto optic modulator, M...Mirror, PBS...Polarizing beam splitter, QWP...quarter wave plate, GS...Galvanometer scanner, BS...Beam splitter, Col...Collimator, FPC...Fiber polarization coupler

As can be seen in Fig. 12, 90% of the light which is emitted from the SLD is coupled into the reference arm. The light in the reference arm is collimated and right at in the beginning of the beam path, two Glan-Thompson polarizer are placed, in order to compensate for dispersion, which is introduced by the polarizers in the sample arm. Then the beam has to traverse two acousto optic modulators which results in a net frequency shift of 3 MHz. This frequency will be the carrier frequency of the corresponding OCT signal [35] [36]. After traversing a PBS and two different glass components for compensating the dispersion introduced by the lenses in the SLO sample arm, a QWP translates the linear polarization state into a circular polarization state. After this the light enters a rapid scanning optical delay line (RSODL), which is responsible for adapting the reference arm length very rapidly. Such a change is essential to correct for axial movements of the eye and is part of the axial eye tracking system which details can be found in [37]. The RSODL

consists of a grating, a lens and a galvanometer scanner. A detailed explanation of this setting is explained in [38]. The light is backreflected from the RSODL and on the way back it passes the QWP again. Therefore the light will be in a linear polarization state, that is perpendicular to the incident polarization state and the beam gets reflected at the PBS, which sends the light to the depth scanner (M-415 Precision Translation Stage, Physik Instrumente), where two mirrors M1 and M2 are mounted. Two mirrors are necessary for maintaining a high coupling ratio of the light into the single mode fiber at the detection unit during movements of the depth scanner. Independent of the translation stage position the beam should always propagate in the same direction. In the previous system only one mirror was used on the translation stage for depth scanning (cf. Fig. 17 A). Therefore the amount of light that was coupled into the single mode fiber was depending on the position of the depth scanner especially in the case where two different detection channels are used. In order to quantify this effect the power that was coupled into the single mode fiber was measured with a power meter (Thorlabs Inc.) while the depth scanner was moving a long distance (several mm). Thereby power changes of some μW was detected. The average power that was coupled into the fiber is about $20\mu\text{W}$. Therefore, the power loss that is detected during scanning corresponds to 20% or more which is unacceptable. Therefore an additional mirror was implemented (c.f. Fig. 17 B). With this improved constellation the beam does not change its direction and the same coupling efficiency is maintained throughout the entire scanning range of the translation stage. In the new reference arm the light gets divided by a 50:50 BS into the co- and cross-polarized channel, before it is coupled into the single mode fibers. Both light components of the reference arm are then brought to interference with the corresponding light from the sample arm which is delivered by an 8m long single mode fiber. The interference signals are detected by two identical balanced detectors and recorded by a data acquisition card with an operating rate of 20 Mega samples per second.

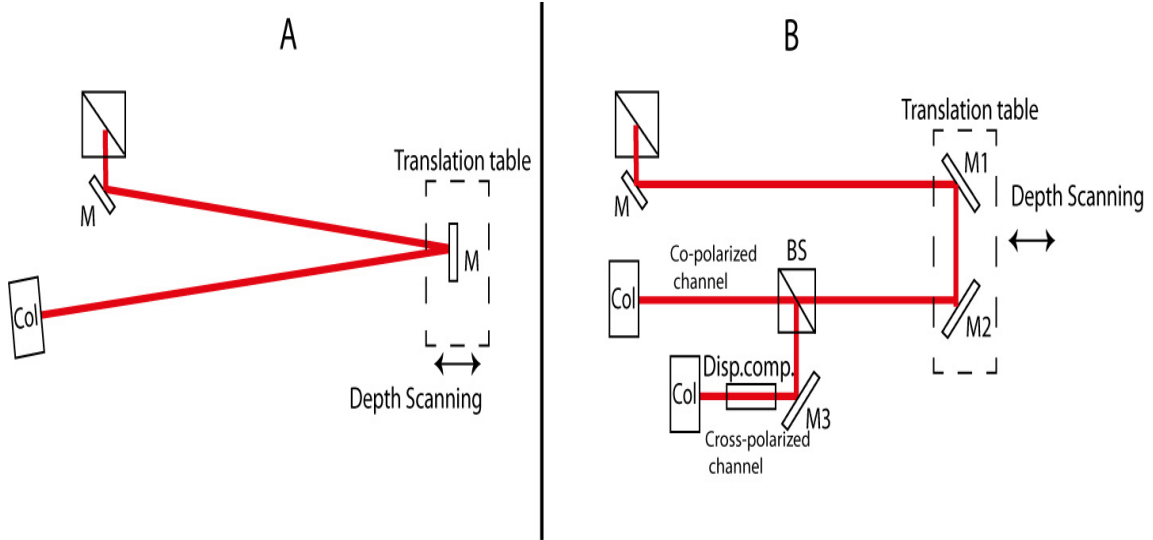


Figure 17: Different configurations of the reference arm. (A) Old setup: only one mirror is mounted on the translation stage for depth scanning. (B) Present setup: The use of two mirrors, enables the independence of the beam direction from the position of the translation stage and allows a constant coupling into the single mode fiber.

After implementation of the new reference arm configuration the power measurements during depth scanning were repeated and still showed power changes. These resulted from the voice coil translation stage, which did not move smoothly in the scanning direction but showed some kind of wobbling. Due to this the coupling efficiency was not constant. For this reason the voice coil translation stage was replaced with a precision translation stage, the M-415.DG (Physik Instrumente). This stage supports a travel range of up to 150mm . The minimal incremental motion of this stage is $0.1\ \mu\text{m}$ [39]. The translation stage is controlled by the C-860 Mercury DC Motor Controller manufactured by Physik Instrumente and corresponding software was developed to enable a synchronized motion for the OCT data acquisition.

3.3.1 Cross Polarization Channel

The cross polarized light of the sample arm has to travel twice through the dispersion compensator and a 90:10 fiber beam splitter (cf. Fig. 12), while the co-polarized light traverses the dispersion compensation and the fiber optic beam splitter only once. Therefore additional material has to be introduced into the beam path of the cross-polarized channel, only to match the dispersion between reference and sample arm of the interferometer of the cross polarized light. Hence, the same glass rods and an identical 90:10 splitter were implemented into the reference arm of this channel. Since both coherence gates have to be at the same position, the collimator in this channel was built on a manual translation stage. This allows for adjusting the path

length. Finally, polarization paddles are implemented in the final fiber optic 50:50 beam splitter of the Mach Zehnder interferometer in order to match the polarization state of the light returning from the reference and sample arm, respectively. This can be easily done by rotating the paddles while maximizing the interference signal. Note that although in both arms a linear polarization state is coupled into the single mode fibers, this polarization state will be changed because of the propagation within the fiber.

3.4 System Performance

In order to obtain good results and maximum sensitivity, optical losses have to be minimized and the dispersion between reference and sample has to be matched. Compared to the previous configuration [10] 50% of the light in the reference arm is used for the cross-polarized channel which leaves only 50% of the light for the co-polarized light. Therefore, the optical throughput in the reference arm has to be optimized in order to obtain sufficient power in both reference arms to reach the shot noise limit of the system. Table 3 summarizes the light powers that were measured at different locations in the reference arm.

Table 3: Measured optical power at different locations in the reference arm. QWP... quarter wave plate, GS... Galvo scanner, RSODL...Rapid scanning optical delay line, M2...Mirror, BS...Beam splitter, Coll... collimator, SM...single mode fiber, BD...Balanced detector

At collimator entry	8.6 mW
After QWP	3.4 mW
At GS of the RSODL	1.9 mW
Before M2	0.800 mW
Before BS	0.430 mW
Before Co-pol Coll	0.200 mW
Before Cross-pol Coll	0.140 mW
Co-pol coupled light into SM fiber measured before the BD	0.022 mW
Cross-pol coupled light into SM fiber measured before the BD	0.015 mW

At the end a maximum power returning from the reference arm of $22 \mu\text{W}$ was measured in the co-polarized channel after coupling into the single mode fiber and $15 \mu\text{W}$ in the cross-polarized channel. In order to match the reference power in both interferometer the power in the co-polarized channel was reduced to $15 \mu\text{W}$ by slightly miss-aligning (tilting) the collimator that is attached to the single mode fiber.

Noise and Sensitivity

Like every imaging process, OCT suffers from different noise sources, which can be subdivided into three classes: the excess noise, the shot noise and the receiver noise [40]. The latter is the so called thermal noise of the receiver and can be lowered by cooling the detector. Each monochromatic light source has a small deviation in power. The shot noise is caused by the quantum nature of the photons, which can be described by a poisson distribution of the photons arrival time. Excess noise depends on the Bose-Einstein characteristics of photons of a broadband light source. Considering a white noise characteristic, the variance of the total noise can be described as [40]

$$\sigma_{noise} = \sqrt{\sigma_{shot}^2 + \sigma_{excess}^2 + \sigma_{receiver}^2} \quad (3.1)$$

Detailed noise calculations can be found in R. Leitgeb et al. [40]. To quantify the SNR in the current system, measurements were performed in the model eye consisting of a lens and a sheet of paper as retina. The measured SNR was 48dB which is similar to previously reported values using the same model eye and the same instrument [10].

Procedure to match the dispersion in both interferometer arms

In section 2.1.4 dispersion was already mentioned. In short, differing light frequencies propagate with different velocities through material depending on the propagation constant of the materials. If the dispersion in the reference arm and the sample arm aren't matched accurately, a loss in resolution appears [25]. For this reason glass (BK7) components are added to the reference arm, which compensate the dispersion introduced in the sample arm. In order to find the optimum amount of material that has to be placed in the reference arm the following procedure was performed. First OCT-B-scans of a mirror as sample were recorded with the system (the y-scanner was not activated during this measurement). An example image is shown in Fig. 18A). From this B-scan the central line which corresponds to one A-scan (depth scan) was extracted. An example of such an A-scan is shown in Fig. 18B). From this A-scan the full width at half maximum (FWHM) of the coherence function which is equivalent to the axial resolution was determined. As can be seen in Fig. 23 B) the dispersion imbalance causes a broadening of the coherence function. Then length of the material in the reference arm was varied until a minimum of the coherence function was observed (cf. Fig. 19).

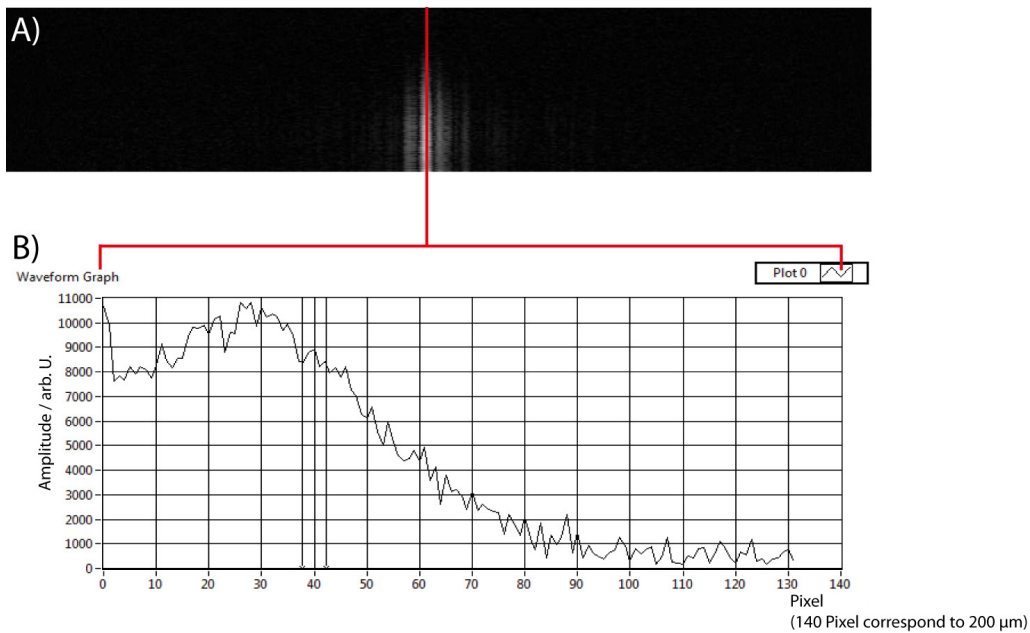


Figure 18: Example images of a mirror as sample for a large dispersion mismatch between both interferometer arms. This image was recorded in the cross-polarized channel. A) OCT B-scan, B) Extracted A-scan at the central location (indicated by the red line in A)

Finally, a resolution of about $8\ \mu\text{m}$ was achieved in the co-polarized channel, which is in good agreement with the theoretical value of $6.5\ \mu\text{m}$ that can be calculated from the FWHM of the emission spectrum of the light source (cf. Eq. 2.12).

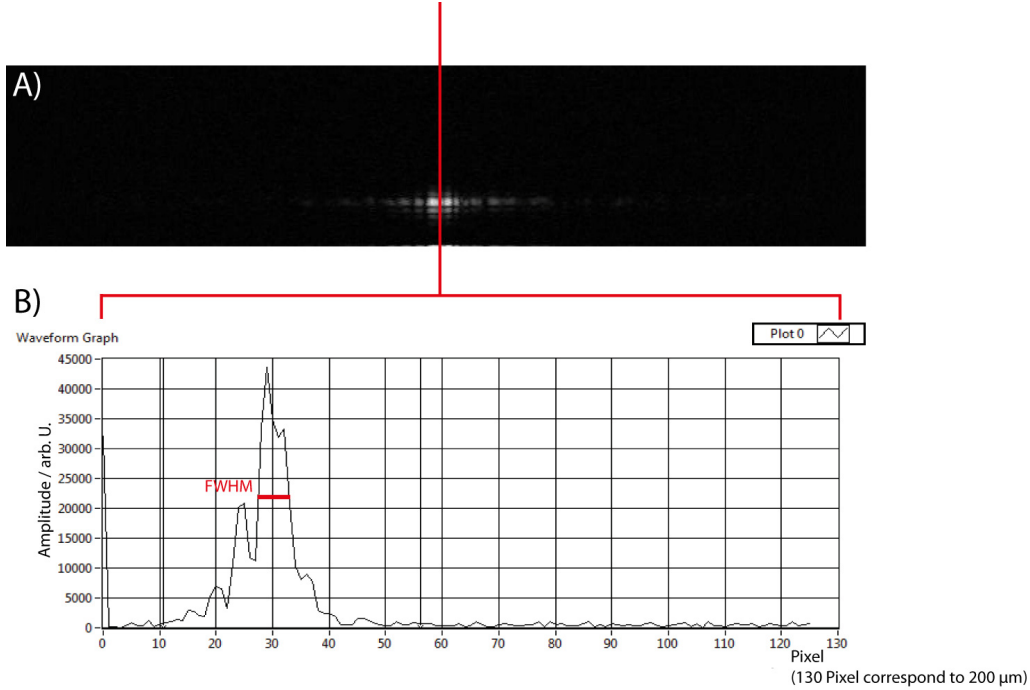


Figure 19: Example images of a mirror when the dispersion between reference and sample arms are matched. The coherence lengths in both channels was below $10\ \mu\text{m}$. A) OCT B-scan B) Extracted A-scan at the central location (indicated by the red line in A)

Measurement of Retardation

Phase retardation was mentioned before in section 2.3. Since two interferometer are used, the location of the coherence gates within the sample may vary. Although any mismatch of the depth location can be eliminated by changing the position of the fiber collimator in the reference arm of the cross polarized channel, jitter and drifts between the interferometer remain. Figure 20 shows the coherence functions obtained from a mirror (a quarter wave plate at 1300nm was placed before the mirror in order to simulate birefringence and introduce retardation of $\sim 41^\circ$) for both polarization channels. Dispersion was compensated for both channels and the reference arm length of the cross polarized channel was adjusted in order to match the length of the co-polarized channel. From the quotient of the amplitudes the retardation can be calculated (cf. Eq. 2.19). For the 1300nm QWP a retardation of 41° was calculated which is in good agreement with the expected value.

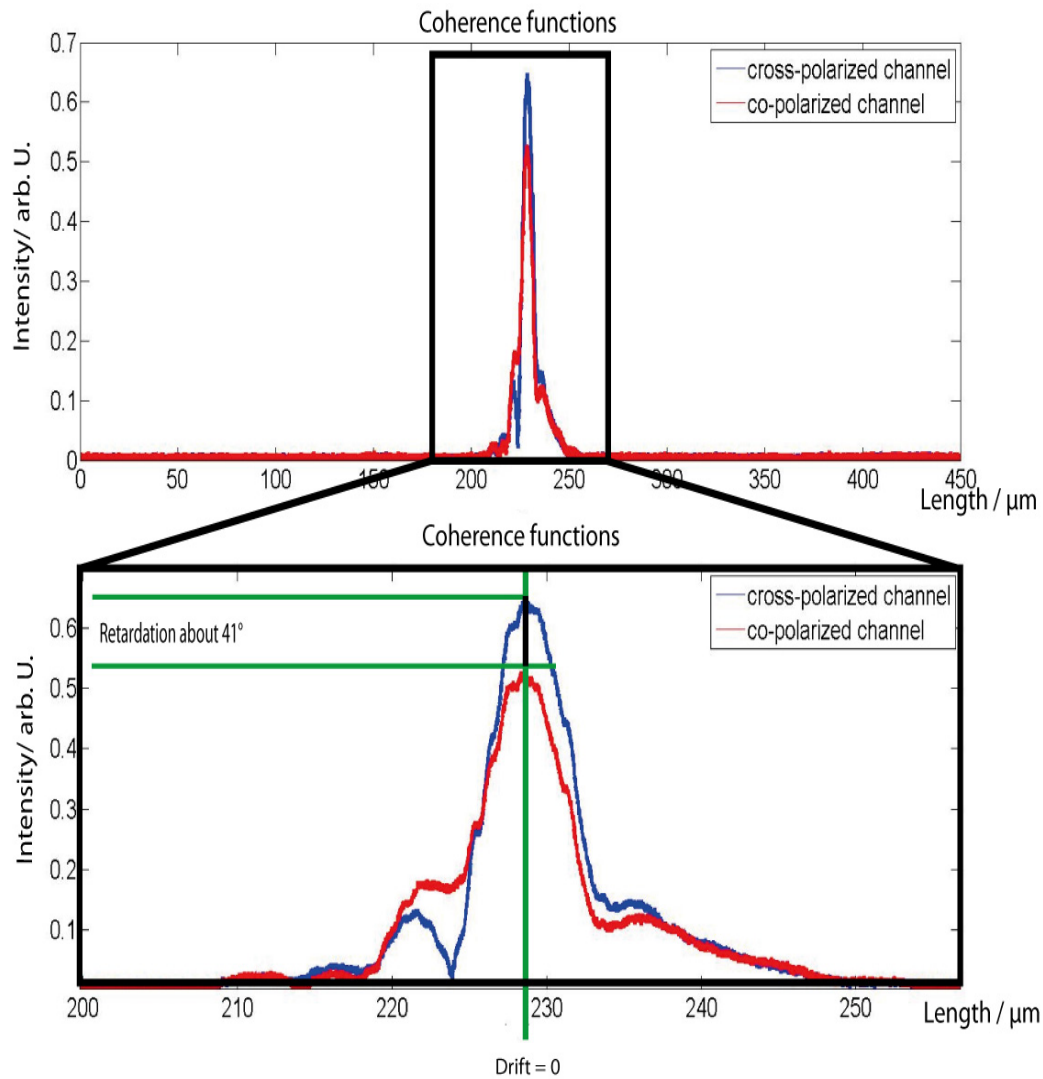


Figure 20: Coherence functions recorded from a mirror as sample and an optimal displacement of $0\mu\text{m}$.: Any displacement in depth causes an high deviation of the calculated retardation. A $\lambda/4$ plate, designed for 1300nm , was implemented in front of the sample mirror which introduces a retardation of 41° .

Since both interferometer share only part of the total beam propagation path environmental factors may influence the optical path length within the interferometer. These include different air circulation or air temperature within the non-common path, since these factors influence the refractive index of air. Hence, the beam path between the PBS and both collimators (cf. Fig. 17) were protected by covering this part of the interferometer with a box. One additional problem are the long fibers that are used in the setup. Any bending of the fiber will introduce birefringence and therefore a change in the optical path length. Therefore the fibers were wrapped over almost the entire length into a foil of aluminium in order to minimize a differing bending of the fibers. After implementing these changes a drift of ($\pm 0.5\mu\text{m}$) with a corresponding retardation error of ($\pm 1^\circ$) could be achieved (cf. Figs. 21 and 22) which seems to be acceptable.

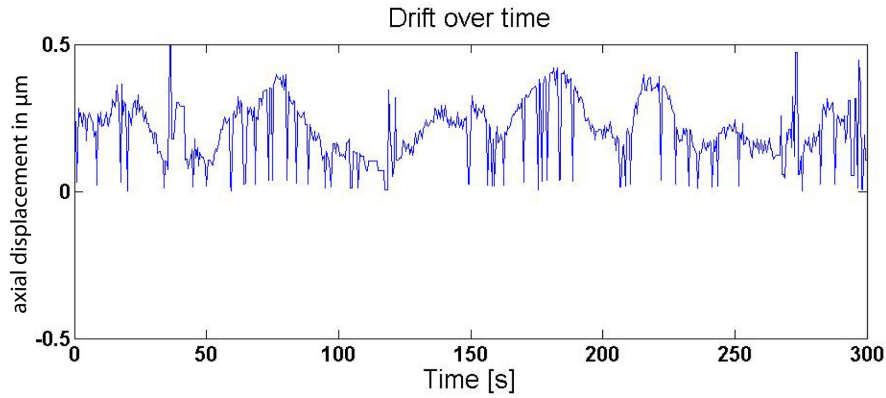


Figure 21: Drift between the axial position of the coherence gate for both polarization channels measured with a mirror as sample: Highest displacement of $0.5\mu\text{m}$ was measured.

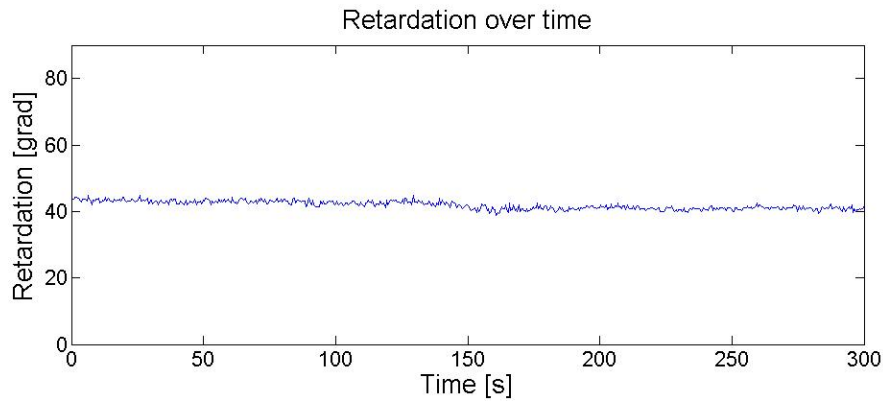


Figure 22: Change of the calculated retardation values caused by the drift between the interferometer arm lengths. Measurements were performed on a mirror as sample and a QWP for 1300nm was placed into the beam path. Variance of $\pm 1^\circ$

4 Results and Discussion

This chapter shows exemplary images of measurements using the modified AO-SLO/OCT setup with polarization sensitivity. Before applying the instrument to in vivo measurements the dynamic focus was calibrated. Thereby the amount of defocus that was introduced by the DM in order to shift the focal plane a certain distance within the tissue has to be determined.

4.1 Calibration of the dynamic focus

In the normal application mode, the AO-loop is used to correct for aberrations. After a good correction is achieved an OCT volume scan is performed. During this scan the coherence gate is shifted rather slowly through the tissue and corresponding en-face images are recorded. In order to shift the focal plane simultaneously with the coherence gate, the shape of the deformable mirror has to be changed, depending on depth range and scanning velocity of the OCT scan. Thereby a conversion factor has to be determined which converts from the shift of the coherence gate (in μm) into a change of the defocus value that is sent to the DM. The dynamic focus should enable to maintain the transversal resolution during OCT volume measurements. In order to achieve this the shape of the deformable mirror is changed continuously, depending on depth range and scanning velocity. The adaptation between the depth scanning speeds (coherence gate and dynamic focus) can be adjusted by a linear calibration factor. After the translation stage was exchanged, the software for measurements (written in Labview) had to be adjusted and the factor needed a new calibration. Figure 23 shows the calibration principle of the system. The model eye for this calibration consists of L2 (30mm lens) and the test resolution target (TRT). The TRT is surrounded by water and simulates the aqueous humor a clear water fluid in the eye. Moving the TRT in axial direction towards the lens, i.e. about 400 μm optically, two observations can be made. First the coherence gate is shifted by 400 μm towards the lens. For this reason a volume scan with a depth range of 400 μm is performed in order to record images from the TRT. Without a dynamic focus this leads to the second observation, i.e. that the SLO and the OCT images appear blurred (due to the limited depth of focus). In order to find the calibration factor, the coherence gate is moved to the new location of the TRT. Then the focus of the DM is changed until a sharp image can be observed. The found defocus value at the DM corresponds then to a 400 μm displacement in the model eye. Once the value was found, a recalculation for the human eye has to be done because instead of a 30mm lens the ideal human eye has a focal distance of 24mm. Taking this into

account the value that was found for the model eye had to be divided by a factor of 4

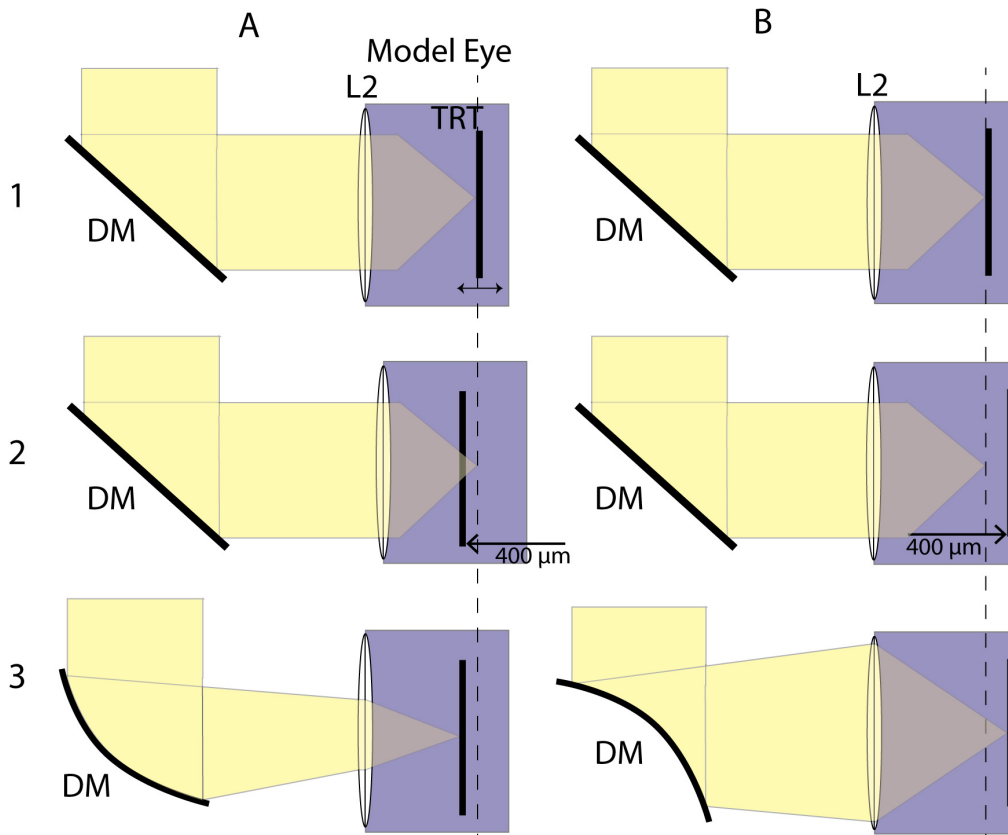


Figure 23: Scheme of the measurements that were performed to calibrate the dynamic focus. A model eye, existing out of a test resolution target TRT in a water bath and a lens L1(30mm) was used. The TRT was mounted on a translation stage that enabled a precise change of the position. A...Different steps to test the positive defocus: 1...TRT is placed in focus position, 2...TRT is moved towards the lens, 3...The shape of the DM is changed until a sharp image is detected. B...Different steps to test negative defocus: 1...TRT is placed in focus, 2...TRT is moved away from the lens, 3...The shape of the DM is changed until a sharp image is detected.

4.1.1 Test resolution target measurements

In order to test the dynamic focus SLO/OCT volume scans were performed in the model eye with the TRT as retina. The first measurement was performed with the TRT placed in the focal plane of the lens. Thereby an SLO/OCT volume scan with a total depth of $400\mu\text{m}$ was recorded. The volume scan started at a depth location of $-400\mu\text{m}$ from the location of the TRT. The coherence gate is then shifted towards the plane of the TRT and en-face images are recorded. Figure 24A shows the en-face images of an imaging plane that corresponds to the plane of the TRT. In a next step the TRT was placed $400\mu\text{m}$ closer to the lens and the volume scan was repeated still without switching the dynamic focus on. As expected the en-face image retrieved from the 3D-data set appears blurred (cf. Fig. 24B). The same measurement was then performed with the dynamic focus switched on which resulted in a sharp image (cf. Fig. 24C). Similar measurements were performed while placing the TRT $400\mu\text{m}$ further away from the focal plane of the lens (the distance from the lens is now focal length $+400\mu\text{m}$). Again, using the dynamic focus, image sharpness can be preserved (cf. Fig. 24D and E)

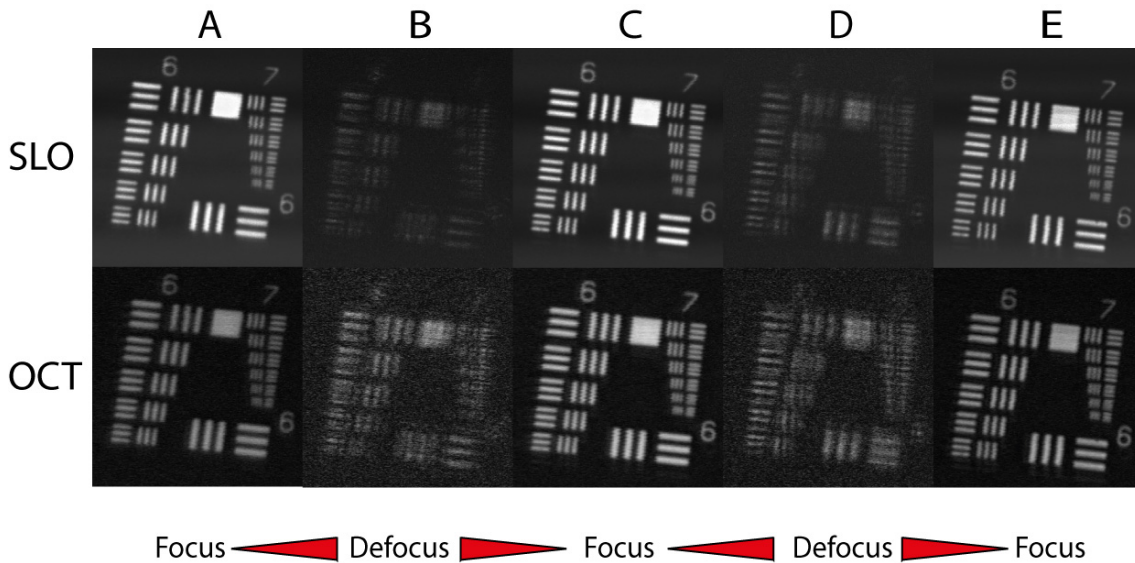


Figure 24: Images of the TRT with different defocus values applied to the DM. Upper scan: SLO images. Lower scans: OCT images. A... Target in focus; B... Target moved $-400\mu\text{m}$ towards the lens; C... Target after applying the additional defocus value to the DM; D... Target moved $+400\mu\text{m}$ in defocus; E... Target after applying the additional defocus value to the DM

4.2 In vivo measurements with dynamic focus

In a next step the dynamic focus scheme was tested for in vivo measurements in order to get high isotropic resolution throughout imaging depth. All in vivo measurements were performed under a protocol that was approved by the ethics committee of the Medical University of Vienna.

4.2.1 Intensity 3D OCT Imaging of human retina

Figure 25 shows an in vivo 3D scan of the retina of a healthy volunteer with a depth range of $600\mu\text{m}$. Because of unintentionally eye motion the 3D recorded volume will have artefacts. These artefacts can be removed in post-processing by using the information in the SLO channel. Although a shift through the retinal layers is introduced by the dynamic focus this shift is rather slow and the change from image frame to image frame is small. Thereby each layer can be correlated to the layer before and the inter frame displacement due to eye motion can be corrected. The coding was done in Matlab and the skeletal structure of the code was written by M. G.-Sicairos [41].

Especially in the en-face projection images the effect of the motion correction can be seen. These corresponding images are much sharper than without motion correction. However, if the SNR of the SLO images is too low, a correlation will lead to erroneous results. As can be seen in the B-scan images (cf. Fig. 25A and C) the entire imaging depth is in focus and imaged sharply.

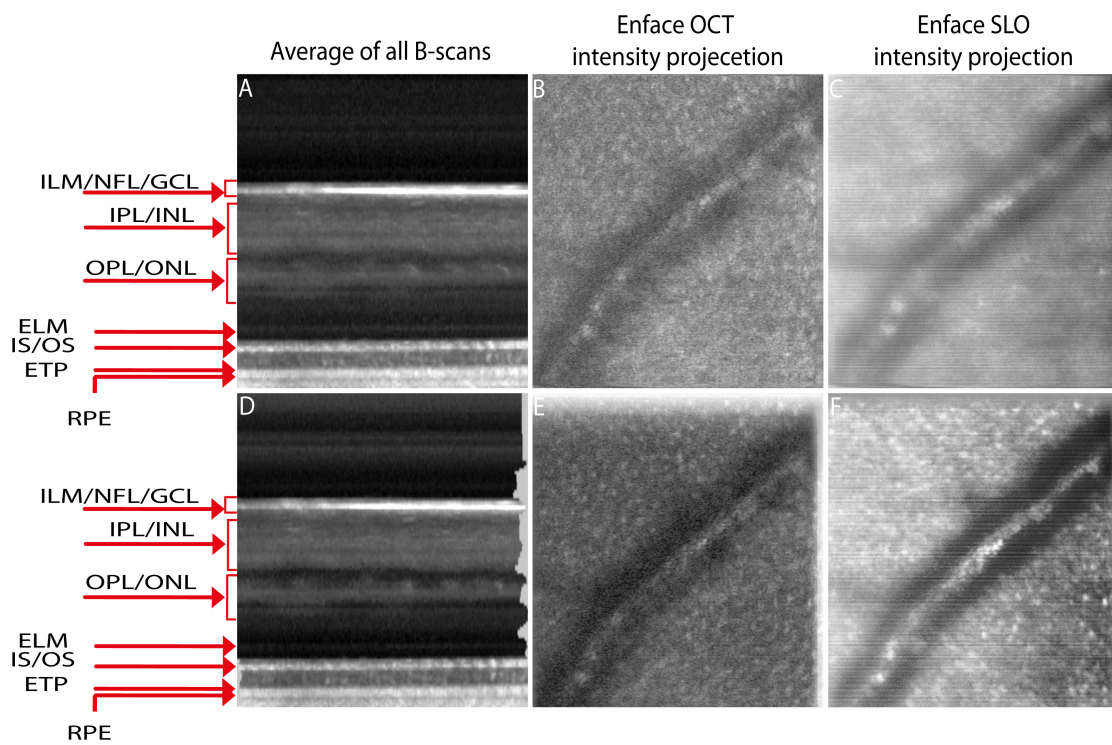


Figure 25: *In vivo* volume measurement with a depth range of $600\mu\text{m}$. A) Z-projection of B-scans of a volume scan of a healthy volunteer without motion correction (MC). B) Enface OCT z-projection image of volume scan without MC. C) Enface SLO image without MC. D) Z-projection of all B-scans of the volume scan after applying MC (note the grey band on the right hand side of the image that results from the inter frame displacements introduced by eye motion) E) OCT and F) SLO z-projection images after applying the MC.

4.3 Comparison between SLO and OCT images

One advantage of the en-face SLO/OCT system is that several images of a certain depth within the retina can be recorded. In order to enhance the SNR these images can be averaged. Fig. 26 shows overview images recorded with the instrument. A more detailed view of the vessels can be seen in Fig. 27 where smaller field of view images with higher resolution are presented. Note the difference between the imaging modalities (SLO and OCT, respectively). While in Fig. 27A only small differences between OCT and SLO image can be seen because the highly reflective nerve fiber layer is imaged. Fig. 27B shows severe differences between both imaging modalities because of the much higher axial resolution provided by OCT. The SLO detects mostly the reflection of the upper vessel wall, but neither the centre nor the bottom of the vessel. With OCT the influence from this highly backscattering layer can be entirely removed because of the coherence gating. The provided axial resolution of about $4.5\mu\text{m}$ of the OCT in tissue allows an explicit separation among the different structures, resulting into an increased contrast of the capillaries. This makes it possible to see even blood flow. In Fig. 27E the bottom of the vessel wall was recorded and also the surrounding structure changed significantly. Due to the higher axial resolution of the OCT much more information can be obtained.

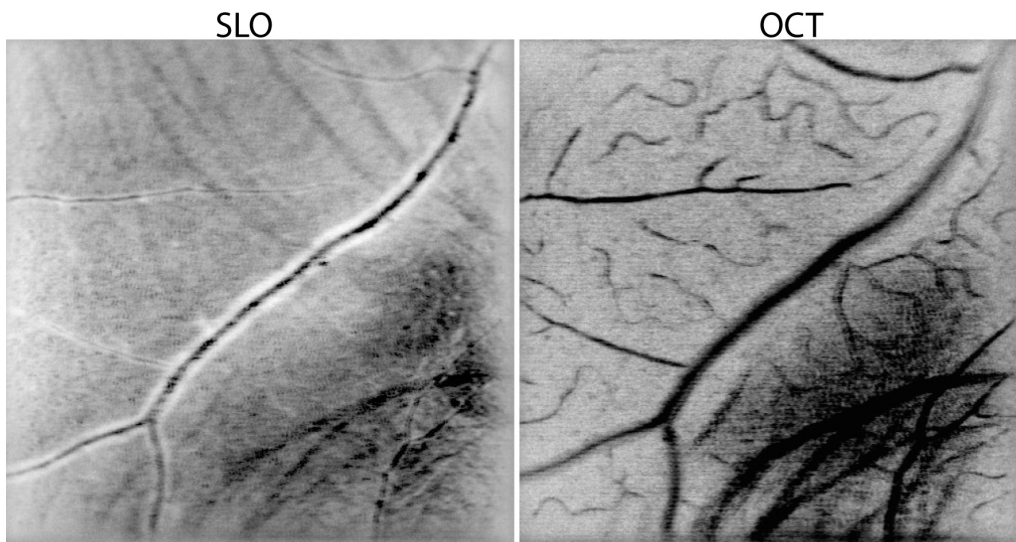


Figure 26: Overview images of vessel structure(Field of view $4^\circ \times 4^\circ$) of a healthy volunteer. The images are an average of 100 images.

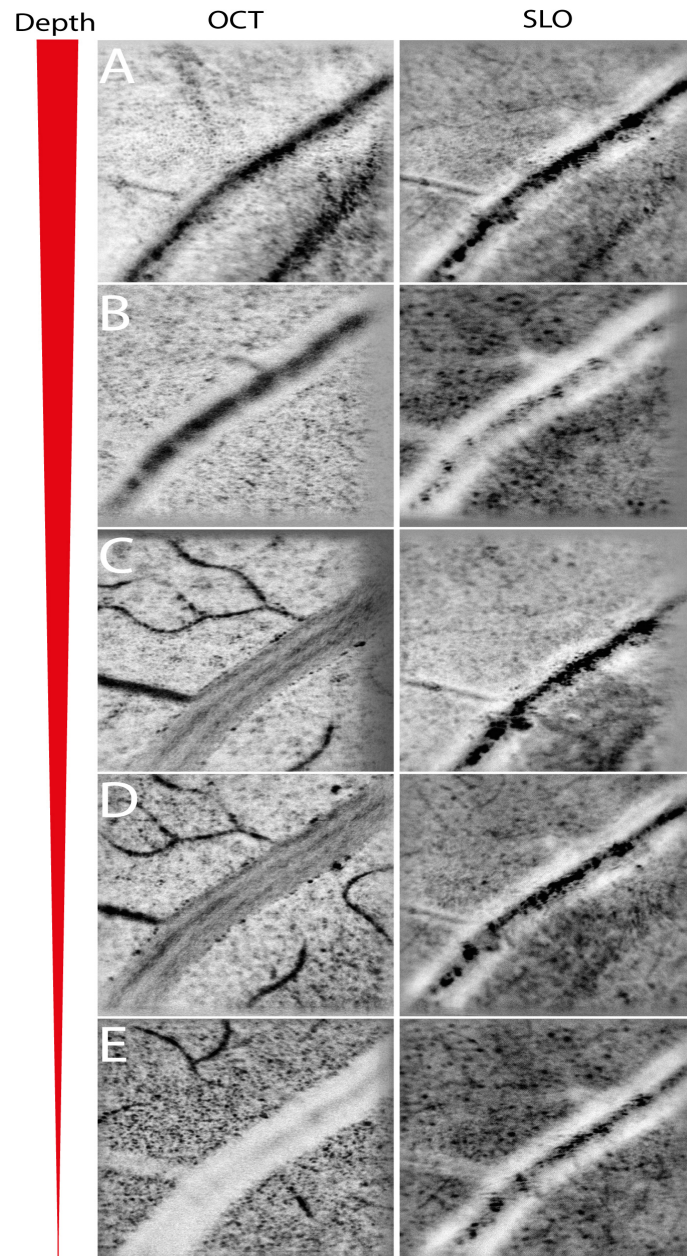


Figure 27: Single layers of the retina recorded at different depths at about 8 degrees temporal from the fovea and a field of view of $1^\circ \times 1^\circ$. A) Top of the vessel. B) Slightly above the vessel. C) and D) Focus on the center of the vessel. E) Images recorded slightly below the vessel.

4.4 Polarisation sensitive images

As mentioned earlier, the system was modified by adding an additional channel for PS-OCT. In the following different image examples with the PS-OCT are presented.

4.4.1 Image of a birefringent test sample

In order to compare the results of the new instrument with state of the art PS-OCT a birefringent material (plastic spoon) was investigated with a working PS-Fourier Domain-OCT built by a colleague. Fig. 28 and 29 show the co-polarized, the cross-polarized, the reflectivity, the retardation and the axis orientation of the test sample. As can be seen in the retardation image by the color change from blue (low retardation) to yellow/red (high retardation) and back to blue, the sample is highly birefringent. Due to the 2π ambiguity of the algorithm the retardation values goes back to 0 whenever the total retardation exceeds 90° . This ambiguity causes also the jump in the axis orientation (cf. Fig. 29) although the birefringent axis remains constant. Note that the FD-OCT system has a much larger field of view and a poorer transverse resolution ($\sim 20\mu\text{m}$) compared to the AO-SLO/OCT system. The results of the AO-SLO/OCT system are presented in Fig. 30 and 31. Apart from the different FOV the images look rather similar.

However, there is more change in the axis orientation image. The axis orientation is calculated from the phase difference between the channels.

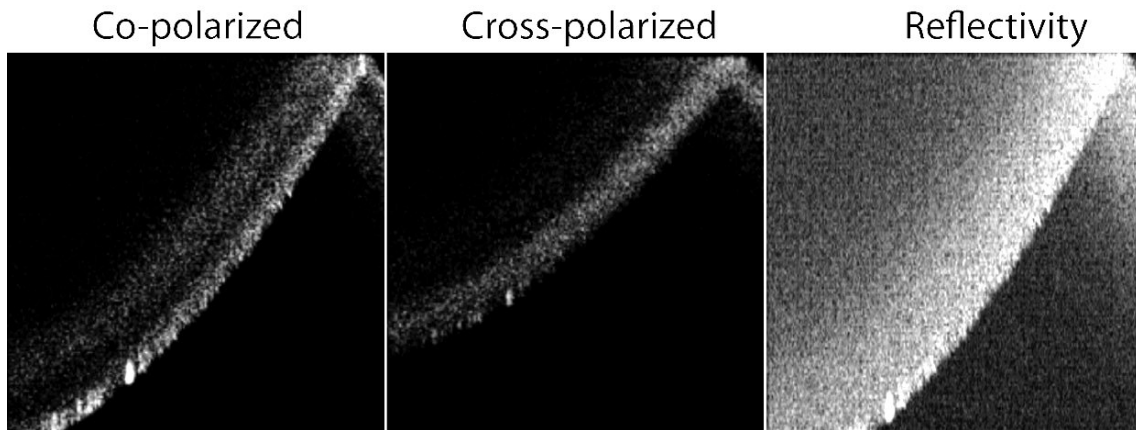


Figure 28: Intensity images of a birefringent material using a FD-PS-OCT setup. Field of view: 2mm lateral and 3.93mm in depth

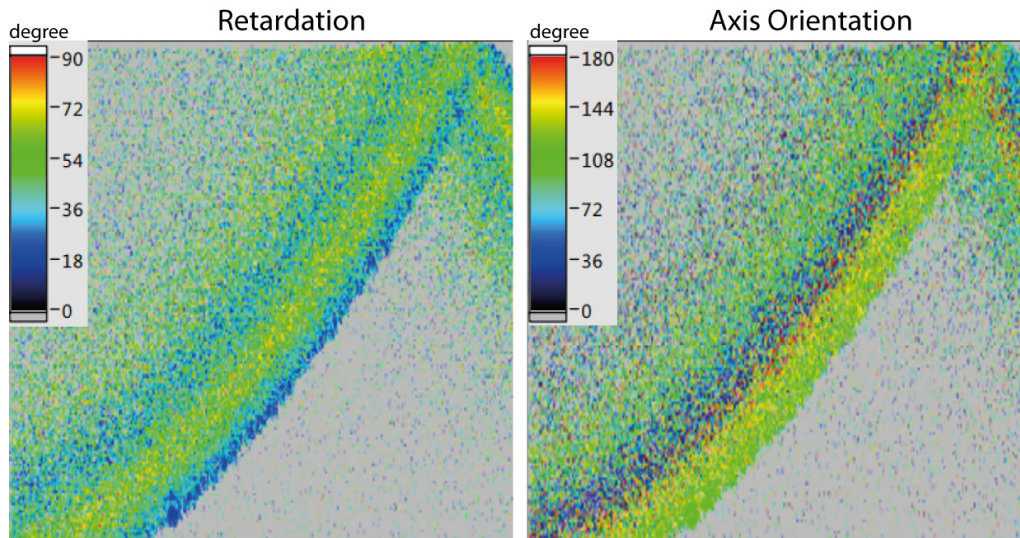


Figure 29: Retardation image and axis orientation images of the birefringent material using a FD-PS-OCT setup (values that are below a certain intensity threshold are displayed in grey). Field of view: 2mm lateral and 3.93mm in depth

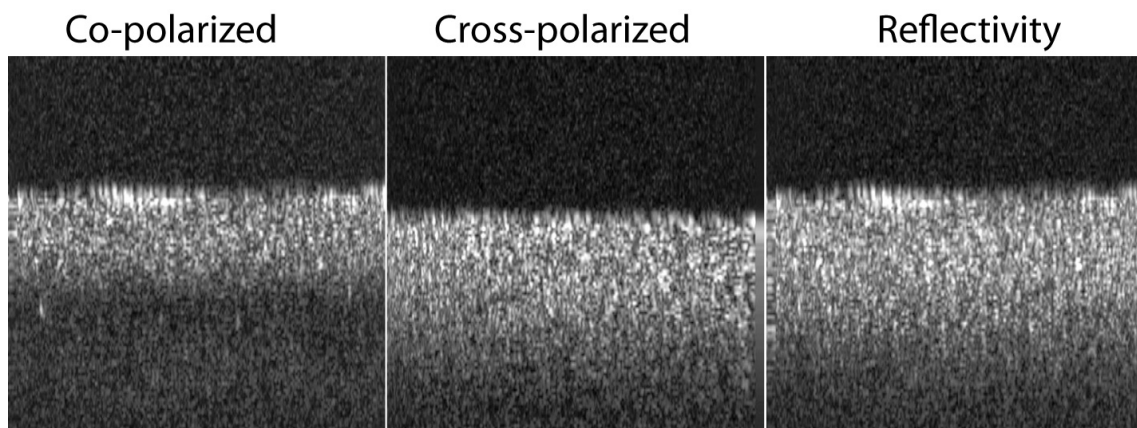


Figure 30: Intensity images of the birefringent test sample recorded with the AO-SLO-PS-OCT system. Field of view: 1° and a depth range of $200\mu\text{m}$.

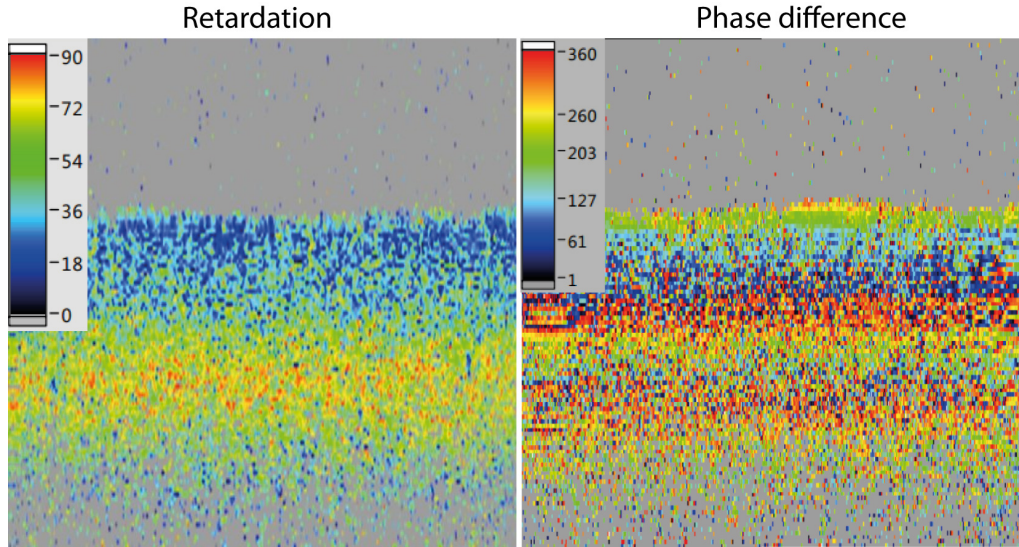


Figure 31: Retardation and phase difference images of the birefringent test sample recorded with the AO-SLO-PS-OCT. Field of view: 1° and a depth range of $200\mu\text{m}$.

4.4.2 PS-OCT of the human retina

The final step was to image the retina of a healthy volunteer. Fig. 32 shows a B-scan, extracted from a volume scan. Unfortunately, the SNR of the images were rather poor. Nevertheless different retinal layers can be distinguished. The retardation image shows depolarizing structures at the level of the RPE similar to conventional PS-OCT [27]

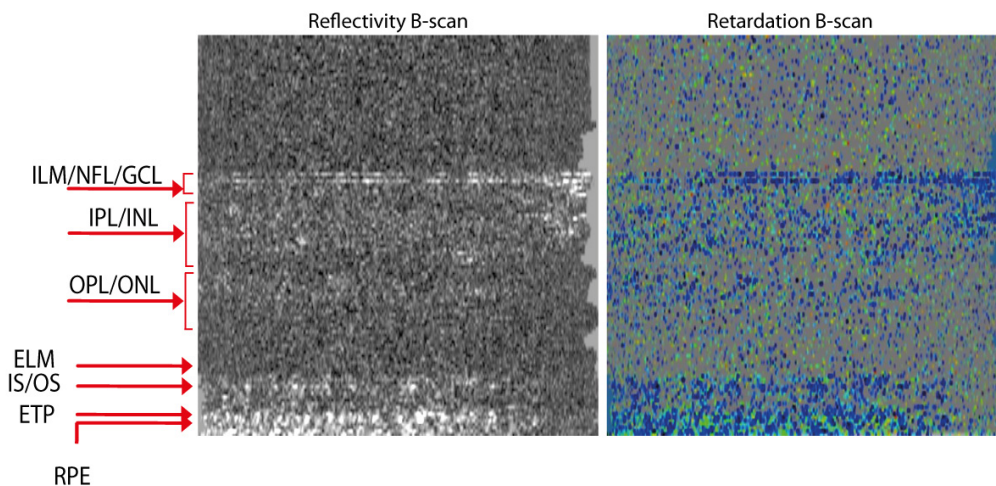


Figure 32: Images of the retina of a healthy volunteer recorded with the AO-SLO-PS-OCT system. Left: reflectivity image (B-scan) extracted from the 3D-dataset. Right: corresponding retardation image (values below a certain intensity threshold are displayed in grey). Same color scale as in Fig. 31

In order to better visualize the depolarizing effect of the RPE Fig. 33 shows the

extracted en-face scans of the photoreceptors (PR) and RPE layer, respectively. While in the PR layer low retardation can be observed, the RPE shows a rather random retardation pattern.

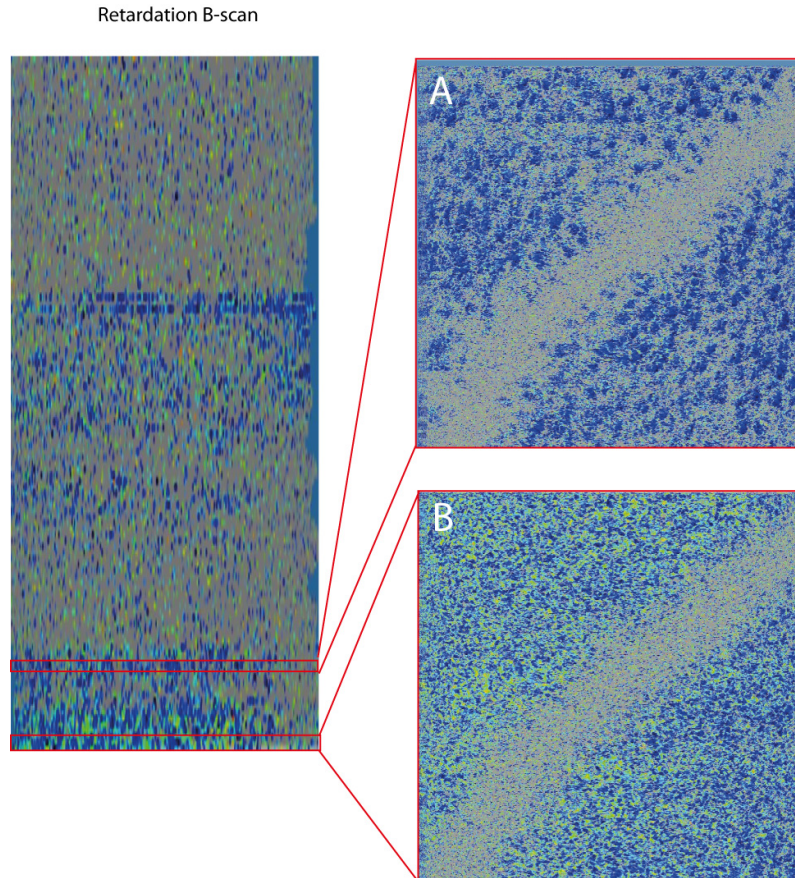


Figure 33: Images of the retina of a healthy volunteer recorded with the AO-SLO-PS-OCT instrument (color scale: same as in Fig.31). Image extension: $1^\circ \times 1^\circ$. A) Photoreceptor layer, B) RPE layer

5 Conclusion

In this thesis an existing adaptive optics scanning laser ophthalmoscope /optical coherence tomography instrument was further developed by improving the dynamic focus capability of the instrument and by implementing a cross-polarization channel for polarization sensitive imaging. The dynamic focus enabled the recording of OCT volumes with high lateral resolution that is maintained throughout imaging depth. Another advantage of the used configuration is the ability to record several images within a certain depth. This allows for an increase of SNR by averaging several similar image frames. Moreover, the instrument allows for a direct comparison between SLO and OCT images. As could be shown in Fig. 27 the superior depth resolution provided by OCT gives completely new insights into retinal structures that are otherwise obscured by highly scattering layers when using AO-SLO alone. The implementation of PS-OCT enables an increased contrast in polarization changing tissue such as the retinal pigment epithelium. However, using PS-OCT the structure of the RPE cells could not be visualized within this thesis. The main contribution to the depolarizing effect comes from pigmented structures as melanin or lipofuscin [42] which are contained in the periphery of the RPE cells. Using dark field illumination schemes these cell structures could be visualized [43] which also seemed to be possible using PS-OCT. One explanation might be that the depolarizing effect in PS-OCT arises from multiple scattering. Since this is a completely random process, the structural information (such as the RPE cell boundary) might get lost and thus prevents the visualization of individual RPE cells. Another problem with the current PS-OCT system is the separation of the cross and co polarized channel into two different interferometer. Because of that phase instabilities occur that influence the measurement of the optic axis orientation. However, within the recording of one image frame (one en-face) image the phase remains rather stable. Therefore a correction of the axis orientation might become possible using post processing algorithms. Although not implemented in this thesis PS-OCT might be used to quantify birefringence introduced by single nerve fiber bundles. This can only be achieved if the transverse resolution of the system is sufficiently high in order to separate individual nerve fiber bundles. Using AO this can be easily achieved. Birefringence of nerve fiber bundles plays a fundamental role in degenerative diseases such as Glaucoma. One severe problem of the current instrument is the low sensitivity. Still losses within the system have to be minimized. Because the system is currently built on two different tables 8 meter long fiber cables have to be used. At the fiber junctions and within the fiber high light losses of the light in the sample arm is expected that degrades the image quality. In order to reach higher SNR these

fibers should be replaced. Furthermore the balanced detectors should be cooled for reducing thermal noise, or replaced by more sensitive detectors. Finally, the system needs to be tested in patients. However, this requires the re-implementation of a fixation target which was removed during this thesis. Here instead of a pellicle for coupling the fixation light into the eye a dichroic mirror might be used which does not influence the polarization state of the light.

References

- [1] A. F. Fercher, W. Drexler, C. K. Hitzenberger, and T. Lasser. Optical coherence tomography - principles and applications. *Reports on Progress in Physics*, 66:239–303, 2003.
- [2] W. Drexler, and J. G. Fujimoto. State-of-the-art retinal optical coherence tomography. *Progress in Retinal and Eye Research*, 27:45–88, 2008.
- [3] D. T. Miller, O. P. Kocaoglu, Q. Wang, and S. Lee. Adaptive optics and the eye (super resolution OCT). *Eye*, 25:321–330, 2011.
- [4] G.J. Tearney, J. F. de Boer, B. Cense, B. H. Park, M. C. Pierce and B. E. Bouma. Improved signal-to-noise ratio in spectral-domain compared with time-domain optical coherence tomography. *Opt. Lett.*, 28(21):2067–2069, 2003.
- [5] R. Leitgeb, C. K. Hitzenberger, and A. F. Fercher. Performance of fourier domain vs. time domain optical coherence tomography. *Opt. Express*, 11(8):889–894, 2003.
- [6] A. G. Podoleanu D. Merino, C. Dainty, A. Bradu. Adaptive optics enhanced simultaneous en-face optical coherence tomography and scanning laser ophthalmoscopy. *Opt. Express*, 14(8):3345–3353, 2006.
- [7] M. Pircher, R. J. Zawadzki, J. W. Evans, J. S. Werner, and C. K. Hitzenberger. Simultaneous imaging of human cone mosaic with adaptive optics enhanced scanning laser ophthalmoscopy and high-speed transversal scanning optical coherence tomography. *Opt. Lett.*, 33(1):22–24, 2008.
- [8] M. Pircher, B. Baumann, E. Goetzinger, H. Sattmann, and C. K. Hitzenberger. Simultaneous SLO/OCT imaging of the human retina with axial eye motion correction. *Optics Express*, 15:16922–16932, 2007.
- [9] M. Pircher, E. Götzinger, H. Sattmann, R. A. Leitgeb, and C. K. Hitzenberger. In vivo investigation of human cone photoreceptors with SLO/OCT in combination with 3D motion correction on a cellular level. *Optics Express*, 18:13935–13944, 2010.
- [10] F. Felberer, J.-S. Kroisamer, B. Baumann, S. Zotter, U. S-Erfurth, C. K. Hitzenberger, and M. Pircher. Adaptive optics SLO/OCT for 3D imaging of human photoreceptors in vivo. *Optics Express*, 5(2):439–456, 2014.

- [11] M. Pircher, E. Götzinger, R. Leitgeb, H. Sattmann, O. Findl, and C. K. Hitzenberger. Imaging of polarization properties of human retina in vivo with phase resolved transversal PS-OCT. *Optics Express*, 12:5940–5951, 2004.
- [12] B. Cense, W. H. Gao, J. M. Brown, S. M. Jones, R. S. Jonnal, M. Mujat, B. H. Park, J. F. de Boer, and D. T. Miller. Retinal imaging with polarization-sensitive optical coherence tomography and adaptive optics. *Optics Express*, 17:21634–21651, 2009.
- [13] Peter Hartmann. Retina layers. http://de.wikipedia.org/wiki/Datei:Retina_layers.svg. [Online; accessed 13-October-2014].
- [14] A. Kampik, and F. Grehn. *Augenärztliche Differenzialdiagnose*. Thieme, second edition.
- [15] M. R. Hee, D. Huang, E. A. Swanson, and J. G. Fujimoto. Polarization-sensitive low-coherence reflectometer for birefringence characterization and ranging. *Journal of the Optical Society of America B-Optical Physics*, 9:903–908, 1992.
- [16] J. F. deBoer, T. E. Milner, M. J. C. vanGemert, and J. S. Nelson. Two-dimensional birefringence imaging in biological tissue by polarization-sensitive optical coherence tomography. *Optics Letters*, 22:934–936, 1997.
- [17] M. Pircher, C. K. Hitzenberger, and U. Schmidt-Erfurth. Polarization sensitive optical coherence tomography in the human eye. *Progress in Retinal and Eye Research*, 30:431–451, 2011.
- [18] W. Geitzenauer, C. K. Hitzenberger, and U. M. Schmidt-Erfurth. Retinal optical coherence tomography: past, present and future perspectives. *British Journal of Ophthalmology*, 95:171–177, 2011.
- [19] A. F. Fercher. Optical coherence tomography. *Journal of Biomedical Optics*, 1:157–173, 1996.
- [20] D. Huang, E. A. Swanson, C. P. Lin, J. S. Schuman, W. G. Stinson, W. Chang, M. R. Hee, T. Flotte, K. Gregory, C. A. Puliafito, and J. G. Fujimoto. Optical coherence tomography. *Science*, 254:1178–1181, 1991.
- [21] Eugene Hecht. *OPTICS*. Addison Wesley, international fourth edition.

- [22] C. D. N. C. Cdang. Onde electromagnetique. http://commons.wikimedia.org/wiki/File:Onde_electromagnetique.png. [Online; accessed 01-August-2014].
- [23] Wikipedia User: Stannered. Diagram of the double-slit experiment. http://en.wikipedia.org/wiki/Double-slit_experiment#mediaviewer/File:Doubleslit.svg. [Online; accessed 01-October-2014].
- [24] M. Born, E. Wolf. *Principles of Optics: Electromagnetic Theory of Propagation, Interference and Diffraction of Light*.
- [25] C. K. Hitzenberger, A. Baumgartner, W. Drexler, and A. F. Fercher. Dispersion effects in partial coherence interferometry: Implications for intraocular ranging. *Journal of Biomedical Optics*, 4:144–151, 1999.
- [26] Public domain. <http://de.wikipedia.org/wiki/Polarisation>. [Online; accessed 18-October-2014].
- [27] E. Götzinger, M. Pircher, and C. K. Hitzenberger. High speed spectral domain polarization sensitive optical coherence tomography of the human retina. *Opt. Express*, 13:10217–10229, 2005.
- [28] C. K. Hitzenberger, E. Götzinger, M. Sicker, M. Pircher, A. F. Fercher. Measurement and imaging of birefringence and optic axis orientation by phase resolved polarization sensitive optical coherence tomography. *Opt. Express*, 9(13):780–790, 2001.
- [29] Dipl. Phys. Bettina Heise. *Phase-sensitive Imaging and Image Processing for Optical Coherence Tomography Applications*. PhD thesis, Institut für Wissensbasierte Mathematische System, Zentrum für Oberflächen- und Nanoanalytik, Mai 2010.
- [30] W. Demtröder. *Experimentalphysik 2 - Elektrizität und Optik*. Springer Verlag, 6th edition edition.
- [31] M. Lombardo, S. Serrao, N. Devaney, M. Parravano, and G. Lombardo. Adaptive optics technology for high-resolution retinal imaging. *Sensors-Basel*, 13:334–366, 2013.
- [32] F. Felberer, J.-S. Kroisamer, C. K. Hitzenberger, and M. Pircher. Lens based adaptive optics scanning laser ophthalmoscope. *Optics Express*, 20(16):17297–17310, 2012.

- [33] I. E. C. (IEC). Safety of laser products. IEC 60825(IEC,2001).
- [34] Imagine eyes. http://imagine-eyes.com/downloads/ies_res-equ.pdf. [Online; accessed 01-August-2014].
- [35] C. K. Hitzenberger, P. Trost, P. W. Lo, and Q. Y. Zhou. Three-dimensional imaging of the human retina by high-speed optical coherence tomography. *Ppt. Express*, 11(21):2753–2761, 2003.
- [36] M. Pircher, E. Goetzinger, R. Leitgeb, and C. K. Hitzenberger. Transversal phase resolved polarization sensitive optical coherence tomography. *Physics in Medicine and Biology*, 49:1257–1263, 2004.
- [37] M. Pircher, E. Götzinger, H. Sattmann, R. A. Leitgeb, and C. K. Hitzenberger. In vivo investigation of human cone photoreceptors with SLO/OCT in combination with 3D motion correction on a cellular level. *Optics Express*, 18:13935–13944, 2010.
- [38] G. J. Tearney, B. E. Bouma, and J. G. Fujimoto. High-speed phase- and group-delay scanning with a grating-based phase control delay line. *Opt. Lett.*, 22(23):1811–1813, 1997.
- [39] Physik instrumente. <http://www.physikinstrumente.com/en/products/prspecs.php?sortnr=701800>. [Online; accessed 03-August-2014].
- [40] R. Leitgeb, C. K. Hitzenberger, and A. F. Fercher. Performance of fourier domain vs. time domain optical coherence tomography. *OPTICS EXPRESS*, 11, 2003.
- [41] M. G.-S., S. T. Thurman, and J. R. Fienup. Efficient subpixel image registration algorithms. *Opt. Lett.*, 33(2):156–158, 2008.
- [42] B. Baumann, S. O. Baumann, T. Konegger, M. Pircher, E. Gotzinger, F. Schlanitz, C. Schutze, H. Sattmann, M. Litschauer, U. Schmidt-Erfurth, and C. K. Hitzenberger. Polarization sensitive optical coherence tomography of melanin provides intrinsic contrast based on depolarization. *Biomedical Optics Express*, 3:1670–1683, 2012.
- [43] D. Scoles, Y. N. Sulai, and A. Dubra. In vivo dark-field imaging of the retinal pigment epithelium cell mosaic. *Biomedical Optics Express*, 4:1710–2723, 2013.